Modeling and Analysis of Sorbent-Enhanced Reforming for Sustainable Hydrogen Production

Talal Naif A Alharbi, **Professor Francisco Trujillo**

talal.alharbi@kaust.edu.sa, francisco.trujillo@unsw.edu.au

Abstract

Sorbent-enhanced reforming (SER) integrates steam methane reforming, water-gas shift and in situ CO_2 capture to enhance hydrogen production while reducing CO_2 in the product gas. The objective of this practicum was to develop and verify connected multi-scale SER models for hydrogen production, CO_2 capture, reactor hydrodynamics, breakthrough behaviour and energy requirements, while establishing a modelling pathway for future integration of experimentally characterised ladle furnace slag (LFS) sorbents. Three linked reactor-modelling frameworks were implemented. First, the published one-dimensional dynamic adiabatic fixed-bed SER model of Mostafa and co-workers was independently reimplemented using ODE and DAE formulations. At the 140-node reference resolution, the DAE reproduced the principal published methane conversion, hydrogen yield and hydrogen purity values generally within approximately one percentage point. Second, the established SER chemistry and non-isothermal treatment were integrated with a Romano-based circulating fluidised-bed framework. Increasing static solids inventory by 50% extended the dense solids-rich region from 3.09 to 7.10 m and increased the carbon capture ratio from 68.80% to 71.68%, while pressure drop increased from 19.8 to 29.8 kPa. Third, a transient reduced-order model was developed for the existing Khalifa University pilot-scale bubbling fluidised-bed reactor. At 873.15 K and $3u_{mf}$, the model predicts pre-breakthrough hydrogen purity, methane conversion and CO_2 capture of 98.419%, 97.763% and 97.806%, respectively, with breakthrough occurring between approximately 213 and 217 min. Benchmarking against the published Di Carlo CFD model reproduced the reported composition trends without parameter tuning. The resulting models establish a numerically verified baseline for future KU experimental validation, LFS sorbent development and larger-scale continuous SER studies.

Date: August 21, 2026

Correspondence: talal.alharbi@kaust.edu.sa

Contents

Nomenclature 2

1 Introduction 3

2 Methodology 4

2.1 Practicum modelling workflow . . . 4
2.2 The reference fixed-bed model . . . 4
2.3 The ODE implementation . . . 5
2.4 The DAE implementation . . . 6
2.5 Governing physics, kinetics and property treatment . . . 7
2.6 Development grids . . . 9
2.7 Integration of the SER-CFB model . . . 9
2.8 The KU pilot-scale bubbling fluidised-bed model . . . 11
2.9 Numerical verification across the three models . . . 14

3 Results 15

3.1 Final fixed-bed benchmark at the reference grid . . . 15
3.2 Circulating fluidised-bed (SER-CFB) results . . . 20
3.3 KU pilot-scale bubbling fluidised-bed (BFB) results . . . 23

4 Discussion 31

4.1 What the progression between models actually established . . . 31
4.2 Interpreting the fixed-bed benchmark . . . 31
4.3 Significance of the circulating-bed inventory result . . . 31
4.4 Why the CFB and KU models must remain separate . . . 33

5 Limitations and Future Work 33

5.1 Limitations of the fixed-bed models . . . 33
5.2 Limitations of the SER-CFB model . . . 34
5.3 Limitations of the KU BFB model . . . 35
5.4 Future work . . . 36

6 Conclusion 37

References 38

A Governing equation groups by model 40

B Fixed-bed equation-to-code map 40

C SER-CFB equation-to-code map 41

D KU BFB equation-to-code map 41

E Major input parameters 42

Nomenclature

Table 1 Principal symbols used in this report. Additional symbols are defined where they first appear.

Symbol	Meaning	Units
A	Reactor cross-sectional area	m^2
$a_{v,j}$	Specific external area of solid phase j	m^{-1}
Ar	Archimedes number	–
$C_{g,i}$	Bulk gas molar concentration of species i	mol m^{-3}
$C_{c,i}$	Catalyst-surface concentration of species i	mol m^{-3}
C_s	Sorbent-surface CO_2 concentration	mol m^{-3}
$D_{ae,i}$	Effective axial dispersion coefficient	m^2 s^{-1}
d_b	Bubble diameter	m
d_p	Particle diameter	m
F_i	Molar flow of species i	mol s^{-1}
H_d	Dense-zone height in the riser	m
H_{mf}	Bed height at minimum fluidisation	m
h_{gs}	Gas-solid heat-transfer coefficient	W m^{-2} K^{-1}
$K_{be,i}$	Bubble-emulsion interchange coefficient	s^{-1}
$K_{bc,i}$, $K_{ce,i}$	Bubble-cloud and cloud-emulsion interchange coefficients	s^{-1}
k_{carb}	Carbonation rate constant	s^{-1}
$k_{m,i}$	Gas-film mass-transfer coefficient	m s^{-1}
N	Number of axial discretisation nodes	–
$n_{\mathrm{CaO},0}$	Initial moles of CaO available for carbonation	mol
P	Pressure	Pa (bar in kinetics)
Q_{ext}	External heat supplied at the reactor boundary	W
R_j	Intrinsic rate of reaction j	kmol kg^{-1}(cat) s^{-1}
R_{carb}	Carbonation rate	mol m^{-3} s^{-1}
$R_{be,i}$	Bubble-emulsion transfer rate of species i	mol m^{-3} s^{-1}
T_g, T_c, T_s	Gas, catalyst and sorbent temperature	K
u	Gas velocity	m s^{-1}
U	Superficial gas velocity	m s^{-1}
u_{mf}, u_t	Minimum fluidisation and terminal velocity	m s^{-1}
u_b, u_{br}	Absolute and relative bubble rise velocity	m s^{-1}
W_s	Total solids inventory	kg
X	CaO conversion to $CaCO_3$	–
$X_{\max}$	Fast-stage limit of sorbent conversion	–
z	Axial coordinate	m
δ	Bubble holdup	–
ε	Bed void fraction	–
ε_{mf}	Voidage at minimum fluidisation	–
$\varepsilon_s(z)$	Local solids volume fraction	–
η	Catalyst effectiveness factor	–
$\eta_c(z)$	Axial carbonation contact factor	–
ν_{ij}	Stoichiometric coefficient of i in reaction j	–
ϕ_{cat}, ϕ_{sorb}	Catalyst and sorbent volume fractions in solids	–
ρ_g, ρ_p	Gas and particle density	kg m^{-3}
μ	Gas viscosity	Pa s

Abbreviations. BFB, bubbling fluidised bed; BTt, breakthrough time; CaL, calcium looping; CCR, carbon capture ratio; CFB, circulating fluidised bed; DAE, differential-algebraic equation; GHSV, gas hourly space velocity; KPI, key performance indicator; KU, Khalifa University; LFS,

ladle furnace slag; ODE, ordinary differential equation; SBU, sorbent bed utilisation; SER, sorption-enhanced reforming; SMR, steam methane reforming; WGS, water-gas shift.

1 Introduction

Hydrogen is an important energy carrier and industrial feedstock with a growing role in the decarbonisation of energy-intensive sectors. Steam methane reforming (SMR) is a well-established route for hydrogen production; however, it is strongly endothermic and equilibrium-limited, requiring high operating temperatures and an external heat supply. In addition, CO_2 is generated during reforming and water-gas-shift reactions and must subsequently be separated from the product stream [1, 2].

Sorbent-enhanced reforming (SER) addresses these limitations by integrating steam methane reforming, the water-gas shift (WGS), and in situ CO_2 capture into a single reactor. A solid CO_2 acceptor, commonly calcium oxide (CaO), removes CO_2 from the gas phase through carbonation, shifting the reaction equilibria towards hydrogen formation and increasing methane conversion and hydrogen purity [1, 3]. Carbonation is also exothermic and can partially compensate for the heat required by the endothermic reforming reactions [2].

The performance of SER depends strongly on reactor configuration and sorbent management. In a fixed-bed reactor, the finite sorbent inventory gradually becomes saturated, and the process operates transiently until breakthrough [1, 2]. Circulating fluidised-bed systems can continuously transport solids between reaction and regeneration units, whereas bubbling fluidised beds provide strong gas-solid contact and solids mixing but still experience sorbent saturation when no continuous regeneration loop is present [14–16]. These differences mean that the same reactor model cannot simply be transferred between reactor configurations without modifying the associated hydrodynamics, heat transfer, and sorbent treatment.

This work developed a Python-based SER modelling framework through three connected phases. First, the published one-dimensional dynamic fixed-bed SER model of Mostafa and co-workers was independently reimplemented using ordinary differential equation (ODE) and differential-algebraic equation (DAE) formulations and benchmarked against the published results [1, 2]. Second, the established SER chemistry and energy treatment were integrated with a Romano-based circulating fluidised-bed framework to investigate the effects of solids inventory and solids distribution on reactor performance [14, 16]. Third, a separate model was developed for the Khalifa University (KU) pilot-scale bubbling fluidised-bed reactor, incorporating bubbling-bed hydrodynamics, bubble-emulsion gas exchange, reforming chemistry, CaO carbonation, heat transfer, and transient sorbent exhaustion. The three modelling phases serve different purposes. The fixed-bed work provides a model-to-model benchmark against published reference results. The circulating fluidised-bed model represents a development framework for continuous SER and calcium-looping operation, while the KU bubbling-bed model provides a pilot-scale modelling framework for the available reactor. The KU model was additionally benchmarked against the published bubbling-fluidised-bed CFD model of Di Carlo et al. under matched operating conditions [24]. This comparison provides an independent model-level assessment but does not constitute direct experimental validation of the KU reactor.

Calcium oxide is used as the reference sorbent throughout the present work. Alternative calcium-rich materials, including ladle furnace slag (LFS) [23], are retained as future research directions rather than included in the present quantitative models. Their implementation would require material-specific physical properties, carbonation and calcination kinetics, cyclic capacity [22], and other experimentally determined parameters before reliable reactor predictions could be made.

2 Methodology

2.1 Practicum modelling workflow

The practicum was organised as three connected phases, each of which produced a separate, independently runnable model package. Figure 1 shows the progression and the specific transfers between phases. Two features of that diagram deserve emphasis before the detail. First, what passes from the fixed-bed phase into the circulating fluidised-bed phase is chemistry and energy treatment, not geometry: the reforming kinetics, the catalyst-film formulation and the multi-phase energy balances are carried forward, while the fixed-bed hydrodynamics are discarded entirely and replaced by the carbonator framework. Second, what passes from the circulating fluidised-bed phase into the KU phase is modelling practice rather than hardware. The KU rig is a bubbling bed with no riser and no solids loop, so its hydrodynamics were reconstructed using bubbling-bed correlations, and its sorbent treatment was reconstructed around a well-mixed inventory. The two fluidised-bed models are deliberately kept physically distinct throughout this report.

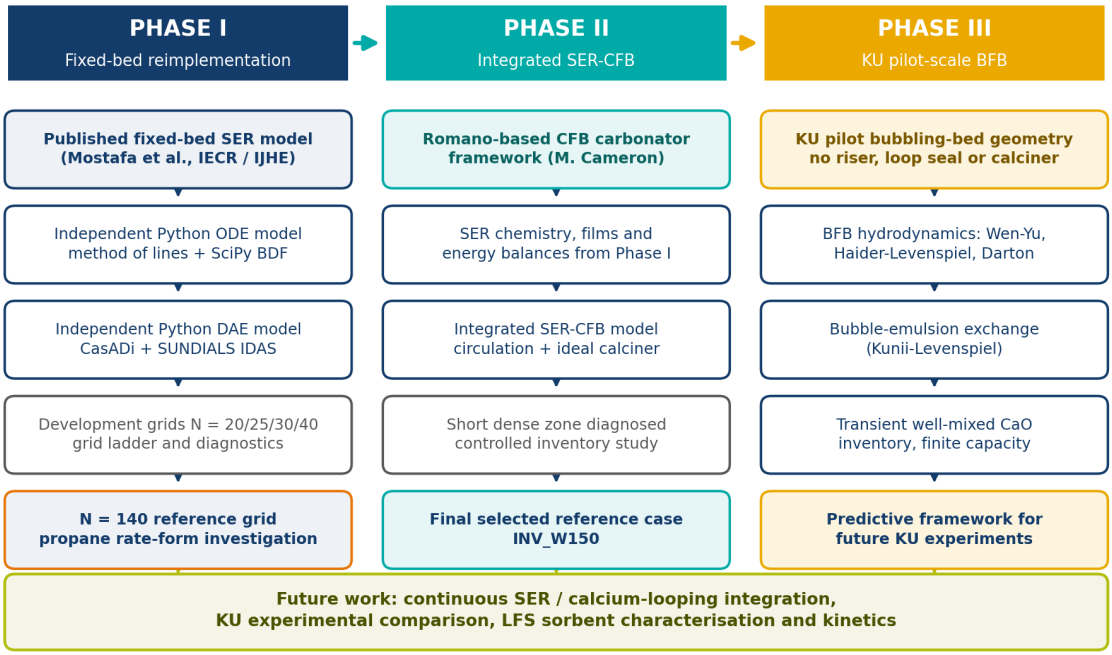


Figure 1 Progression of the practicum across its three phases.

2.2 The reference fixed-bed model

The reference system is an adiabatic fixed-bed reactor operated through the reforming half of a sorption-enhanced cycle. Seven gas species are carried: methane, propane, steam, hydrogen, carbon monoxide, carbon dioxide and nitrogen. The bed contains a nickel reforming catalyst and a calcium oxide sorbent, and, in some cases, a fraction of the sorbent is replaced by dense inert alumina pellets that act as a heat carrier.

The governing balances are partial differential equations in time and axial position. Applying the method of lines replaces the spatial derivatives with finite-difference expressions while retaining the time derivatives, yielding a large coupled system in time. Taking the gas-species balance as the representative case, the continuous form is

Table 2 Operating basis of the reference fixed-bed SER model, as reported in the reference work and its Supporting Information.

Quantity	Value
Reactor internal diameter	2.26 m
Bed length	5 m
Feed temperature	550 °C
Operating pressure	10 bar
Steam-to-carbon ratio	4
GHSV	350 N m^3 h^{-1} m^{-3}
Initial solids temperature	850 °C
Bed void fraction	0.4
Maximum sorbent conversion X_{max}	0.4
Inert heat carrier (when present)	alumina, ρ = 3950 kg m^{-3}, c_p = 0.88 kJ kg^{-1} K^{-1}
Reference spatial discretisation	first-order backward finite differences, 140 axial nodes
Breakthrough criterion	dry outlet CO_2 mole fraction reaches 0.02

$$\varepsilon \frac{\partial C_{g,i}}{\partial t} = -\frac{\partial \left(u\, C_{g,i}\right)}{\partial z} + \frac{\partial}{\partial z}\left(D_{ae,i} \frac{\partial C_{g,i}}{\partial z}\right) - a_{v,c} k_{m,i} \left(C_{g,i} - C_{c,i}\right) - a_{v,s} k_{m,\mathrm{CO_2}} \left(C_{g,\mathrm{CO_2}} - C_s\right) \delta_{i,\mathrm{CO_2}} \quad (1)$$

where the last term applies only to carbon dioxide. The bed is divided into N nodes at $z_k = (k-1)\Delta z$ with

$$\Delta z = \frac{L}{N-1} \quad (2)$$

and the unknown becomes the nodal value $C_{i,k}(t)$. Convection is discretised using first-order upwind differences, and dispersion using central differences, matching the scheme used by the reference implementation. Stacking every species, every temperature, and the sorbent conversion at every node yields a single large system over time.

What happens next is the only structural difference between the two implementations built in this practicum. If the algebraic film balances are eliminated or substituted before integration, the system becomes a pure initial-value problem $\dot{y} = f(t, y)$ and is handed to a stiff ODE solver. If instead the film balances, the pressure relation, the velocity closure and the boundary conditions are retained as algebraic equations carrying no time derivative, the system is a differential-algebraic system $F\left(t, y, \dot{y}\right) = 0$ and is handed to a DAE solver. The physics and the discretisation are the same in both cases.

2.3 The ODE implementation

The ODE model was built first. It integrates $\dot{y} = f(t, y)$ with the SciPy `solve_ivp` driver using the implicit backward-differentiation-formula method, which is necessary because the system is stiff: the inlet reforming layer is sharp, the kinetics depend strongly on temperature, and the carbonation source is localised.

To reach that form, the algebraic relations of the reference model are removed before the state vector reaches the solver. The catalyst film balance

$$a_{v,c}k_{m,i}\left(C_{g,i}-C_{c,i}\right)=-\eta(1-\varepsilon)x_c\rho_c\sum_j \nu_{ij}R_j \tag{3}$$

is not solved. Instead, the catalyst-surface concentration is approximated by the bulk gas concentration,

$$C_{c,i}\approx C_{g,i} \tag{4}$$

on the basis that external film resistance is negligible, which allows the Xu–Froment rates to be evaluated directly from bulk composition and avoids solving a coupled nonlinear algebraic system for all catalyst-surface species at every node and every solver step.

The sorbent film balance is retained but solved analytically, because it involves a single surface variable and is linear in it. Its closed form is

$$C_s=\frac{a_{v,s}k_{m,\mathrm{CO_2}}C_{g,\mathrm{CO_2}}+\beta\, y_{eq}}{a_{v,s}k_{m,\mathrm{CO_2}}+\dfrac{\beta}{C_t}} \tag{5}$$

with

$$\beta=(1-\varepsilon)\,x_s\,\rho_{\mathrm{CaO}}\,\frac{1000}{MW_{\mathrm{CaO}}}\,k_{carb}\,(X_{\max}-X) \tag{6}$$

The velocity follows a quasi-steady closure $u = F/C_{tot}$ rather than a dynamic momentum balance, so it varies locally with total concentration and with the change in molar flow caused by reaction, but it does not carry its own time derivative. The inlet boundary is treated as Dirichlet, which is a good approximation because the grid Péclet number is large. The implementation lives in `ser_model/`, with `reactor.py` assembling the right-hand side, `kinetics.py` holding the rate laws, `nasa_thermo.py` and `thermo.py` the thermodynamics and mixture properties, `transport.py` the correlations, and `postprocess.py` the performance indicators; `results_ODE.py` is the single entry point.

2.4 The DAE implementation

The DAE model is a separate implementation, not a modified copy of the ODE code. It was written to retain the algebraic structure that the reference model actually solves, and it uses a different symbolic framework and a different integrator: the residual system is assembled in CasADi and integrated with SUNDIALS-IDAS.

The system is semi-explicit and of index one. The differential variables are the concentrations of the seven gas species, the gas, catalyst, and sorbent temperatures, and the sorbent conversion. The algebraic variables are the seven catalyst-surface concentrations, the sorbent-surface carbon dioxide concentration, the local pressure and the gas velocity, together with the boundary values at both ends of the bed. The catalyst and sorbent film balances are imposed as written; the pressure follows the Ergun relation [13] discretised by backward differences; the velocity follows a total-mass closure obtained by summing the species balances in which the feed flux equals convection plus back-dispersion, with a zero-gradient condition at the outlet. Because the Danckwerts conditions are algebraic residuals rather than prescribed values, the solver must determine the inlet state simultaneously with every interior node, which is more expensive than the treatment used by the ODE model but closer to the reference formulation.

Consistent initialisation is a real requirement for a DAE and was handled explicitly. A damped Newton solve is applied to the algebraic system at $t = 0$, converging to an infinity-norm residual of

order 10^{-13} in approximately six iterations for every shipped case, followed by the IDAS consistent-initial-condition routine. The implementation lives in `ser_dae/`, with `dae_model.py` assembling the residual; `kinetics.py`, `equilibrium.py`, `thermo.py`, and `transport.py` supplying the chemistry, thermodynamics, and correlations; `boundary_conditions.py` the algebraic boundary rows; and `postprocess.py` the performance indicators. `results.py` is the entry point, and `run_all_parallel.py` runs the independent cases concurrently.

Table 3 Structural comparison of the two independent fixed-bed implementations. The physics and the spatial discretisation are common; the differences are entirely in which relations are eliminated before integration and in the class of solver that follows.

Feature	ODE implementation	DAE implementation
System form	$\dot{y} = f(t, y)$	$F\left(t, y, \dot{y}\right) = 0$, semi-explicit index 1
Symbolic framework	NumPy / SciPy	CasADi
Integrator	SciPy `solve_ivp`, implicit BDF	SUNDIALS-IDAS
Catalyst film	Substituted, $C_{c,i} \approx C_{g,i}$	Algebraic constraint, solved simultaneously
Sorbent film	Retained, solved in closed form	Algebraic constraint, solved simultaneously
Pressure	Ergun integrated for reporting; inlet P used in kinetics	Algebraic local $P(z)$ from Ergun, backward FD
Velocity	Quasi-steady closure $u = F/C_{tot}$	Algebraic total-mass closure
Mixture diffusivity	Wilke form with $\left(1 - y_i\right)$ numerator	SI reciprocal rule
Gas thermal conductivity	Fitted power law	Eucken relation
Initialisation	Direct	Damped Newton plus IDAS consistent initialisation
Entry point	`results_ODE.py`	`results.py`

2.5 Governing physics, kinetics and property treatment

The full set of equations is carried in both implementations. The gas-phase balance shown in subsection 2.2 tracks convection, axial dispersion and exchange with both solids. Three energy balances are solved. The gas energy balance carries and conducts heat, exchanging it with each solid phase, so the gas is the medium that thermally couples the endothermic catalyst to the exothermic sorbent. The catalyst energy balance accounts for the heat of reactions occurring on the catalyst, whose endothermicity produces the cold front at the inlet. The sorbent energy balance includes the carbonation exotherm, which drives the travelling high-temperature reaction zone, and accounts for changes in sorbent density and heat capacity as calcium oxide converts to calcium carbonate. When inert pellets are present, a fourth balance carries their thermal ballast [1, 2].

Sorbent conversion evolves according to

$$\frac{dX}{dt} = MW_{\mathrm{CaO}}\, R_{carb} \tag{7}$$

with the carbonation rate proportional to the excess of carbon dioxide over its equilibrium value and to the remaining capacity $(X_{\max} - X)$, so that capture ceases as conversion approaches $X_{\max} = 0.4$ [1].

The catalytic chemistry uses the Xu–Froment rate laws [3], whose numerators express the distance from equilibrium so that the same rate law runs in either direction, divided by the square

of a competitive adsorption denominator

$$DEN = 1 + K_{CO}p_{CO} + K_{H_2}p_{H_2} + K_{CH_4}p_{CH_4} + K_{H_2O}\frac{p_{H_2O}}{p_{H_2}} \tag{8}$$

The steam methane reforming rate takes the form

$$R_1 = \frac{k_1}{p_{H_2}^{2.5}} \frac{\left(p_{CH_4}p_{H_2O} - \dfrac{p_{H_2}^3 p_{CO}}{K_1}\right)}{DEN^2} \tag{9}$$

with analogous expressions for the global reforming and water-gas-shift reactions. Rate constants follow Arrhenius forms and adsorption constants van 't Hoff forms, both referenced at 648 K, and the equilibrium constants closing the numerators come from the Twigg polynomials [4]. Reaction enthalpies at 298 K are +206.1, +165.0 and −41.15 kJ mol^{-1} for steam reforming, global reforming and the shift, and −178 kJ mol^{-1} for carbonation [2–4].

Propane co-feeding uses the Uskov macrokinetic rate. This is the propane kinetic expression and is entirely separate from the shift chemistry; the Xu–Froment water-gas shift always remains in the model and continues to govern the carbon monoxide produced by methane reforming. The reaction to which the Uskov parameters were fitted is the lumped overall conversion [5]

$$C_3H_8 + 6\,H_2O \rightarrow 3\,CO_2 + 10\,H_2 \tag{10}$$

In the original experimental work carbon monoxide remained below the reported detection level and was deliberately excluded from the proposed macrokinetic scheme, so the fitted parameters describe overall propane conversion rather than an independent propane-to-carbon-monoxide reforming step. The propane reaction form implemented here is therefore matched to the rate law to which it was fitted [3, 5].

Transport follows the correlations of the reference Supporting Information: Pfeffer for gas-solid mass and heat transfer in a packed bed [10], Wakao for effective axial dispersion [11], Fuller for binary diffusivities combined into mixture diffusivities [12], Specchia for effective axial thermal conductivity, and Ergun for pressure drop [13]. A solid thermal conductivity of 1.0 W m^{-1} K^{-1} is assumed because the reference material does not state it.

Thermodynamics uses two-range NASA-7 polynomials for the gas species and Kelley correlations for the solids, so every reaction enthalpy in the energy balances is temperature-dependent and Kirchhoff-consistent [8]. The methane coefficients were verified digit-exact against the GRI-Mech 3.0 database, and a high-temperature regression suite in `ser_dae/test_thermo_high_T.py` guards them. The overall SER reaction enthalpy runs from about −13.6 to +13.7 kJ mol^{-1} across the operating range, against −13.5 to +13.2 kJ mol^{-1} reported by the companion paper.

Because the Multiflash package used by the reference work was unavailable, five properties were computed from explicit correlations instead [9]: mixture molecular weight from composition, density from the ideal-gas law, heat capacity from the same NASA-7 polynomials used for the thermodynamics, viscosity from a power law combined by the Herning–Zipperer square-root-of-molar-mass rule, and thermal conductivity from the Eucken relation in the DAE and a fitted power law in the ODE, again combined by the Herning–Zipperer rule. These substitutions affect the gas-solid heat-transfer coefficient, the axial thermal conductivity, and the Ergun term, and are one identified source of the residual differences reported in subsection 3.1.

Performance indicators follow the reference definitions and are computed by integrating outlet molar flows from start-up to breakthrough: integral methane conversion, integral net hydrogen

yield relative to the theoretical maximum, integral dry hydrogen purity, integral carbon capture ratio with carbon-number weighting, sorbent bed utilisation, and the corresponding hydrocarbon conversion and yield when propane is present. Breakthrough time is the moment the dry outlet carbon dioxide mole fraction first reaches 0.02 on a sustained basis [1].

2.6 Development grids

The number of axial nodes fixes the spatial step through $\Delta z = L/(N-1)$. For the 5 m bed, 40 nodes give $\Delta z = 0.128$ m and 140 nodes give $\Delta z = 0.036$ m. Lower-resolution grids were used during numerical development to reduce computational cost, whereas the final fixed-bed benchmark simulations were performed using 140 axial nodes to match the spatial discretisation of the published reference model [1, 2].

Table 4 Purpose of each axial grid used during the practicum. The final benchmark results are reported only at $N = 140$.

Grid	Purpose
$N = 40$	Principal development grid used for numerical testing and model development
$N = 140$	Reference grid matching the published model; used for the final ODE and DAE benchmark

All final fixed-bed benchmark results reported in subsection 3.1 were generated at $N = 140$, ensuring that differences between the present implementations and the published model are not due to spatial resolution [1, 2].

2.7 Integration of the SER-CFB model

2.7.1 Contributions and attribution

The second phase of the practicum was carried out as part of the broader SER/calcium-looping project team. Matthew Cameron, a member of the project team, contributed the Romano-based circulating fluidised-bed carbonator and hydrodynamic framework used as the starting point for this phase. This framework provided the dense- and lean-zone solids representation, solids-inventory closure, sorbent-circulation treatment, and carbonation-contact formulation, based on Romano's model [14].

In the present practicum, this existing CFB framework was integrated with the SER chemistry and energy treatment developed during the fixed-bed phase. The resulting integrated SER-CFB model incorporated the Xu–Froment reforming kinetics, catalyst gas-film treatment, gas-phase species balances, non-isothermal gas, catalyst and sorbent energy balances, an idealised calciner interface, and loop-energy accounting. The integration, operating-condition studies, numerical verification, and analysis of the final SER-CFB model formed part of the work reported in this practicum.

2.7.2 Model structure

The integrated model is a steady-state, one-dimensional, reduced-order representation of a dilute circulating fluidised-bed riser with continuous catalyst and sorbent circulation. An algebraic ideal calciner is included to close the calcium and energy loops. The CFB hydrodynamic treatment follows the dense/lean representation of Romano and the Kunii–Levenspiel fluidisation framework [14–16].

For each operating case, the methane feed is fixed, and the inlet steam flow is determined from the selected steam-to-carbon ratio:

$$F_{\mathrm{H_2O},in} = \left(\frac{S}{C}\right) F_{\mathrm{CH_4},in}, \qquad F_{tot,in} = F_{\mathrm{CH_4},in}\left(1 + \frac{S}{C}\right) \tag{11}$$

and the superficial gas velocity from the ideal-gas relation $u_0 = F_{tot,in} RT_{in}/(AP)$.

The hydrodynamic calculation is completed before solving the coupled reaction and energy equations. The total solids inventory is used to determine the height of the dense lower region, H_d, through the solids-inventory closure [14]:

$$W_s = A\rho_s \int_0^{H_t} \varepsilon_s(z)\, dz \tag{12}$$

which is solved numerically for H_d rather than being prescribed. Above the dense zone the solids fraction decays exponentially, so that the axial profile is

$$\varepsilon_s(z) = \varepsilon_{s,d},\ z \le H_d; \qquad \varepsilon_s(z) = \varepsilon_s^* + \left(\varepsilon_{s,d} - \varepsilon_s^*\right) \exp\left[-\alpha\left(z - H_d\right)\right],\ z > H_d \tag{13}$$

The resulting solids profile controls the local catalyst and sorbent concentrations and therefore affects reforming, carbonation, gas-solid heat transfer, pressure drop and gas residence time [14–16].

At each axial location, the catalyst-surface composition is determined from an algebraic gas-film balance rather than assumed equal to the bulk-gas composition. The resulting catalyst-surface partial pressures are used in the Xu–Froment reaction-rate expressions [3]. The intrinsic catalytic rates are converted to a volumetric reactor source through

$$r_j^{eff} = 1000\, \eta_{cat}\, \varepsilon_s\, \phi_{cat}\, \rho_p\, r_j \tag{14}$$

Carbonation is computed independently from the local carbon dioxide concentration, its equilibrium value, the local solids fraction, the sorbent fraction, the intrinsic rate constant and an axial contact-efficiency factor:

$$R_c = k_{ri}\, x_{vol}\, \phi_{sorb}\, \varepsilon_s\, \eta_c(z)\left[C_{\mathrm{CO_2}} - C_{eq}\left(T_s\right)\right] \tag{15}$$

with the source set to zero wherever the driving force is non-positive.

The axial gas-species balances are

$$\frac{dF_i}{dz} = A\left[\sum_j \nu_{ij}\, r_j^{eff}\right] - A\, R_c\, \delta_{i,\mathrm{CO_2}} \tag{16}$$

solved as a one-dimensional plug-flow representation with no axial gas dispersion and no gas back-mixing.

2.7.3 Three-phase energy balances and the calciner interface

Separate energy balances are solved for the gas, catalyst, and sorbent phases. The gas exchanges heat with both solid phases and with the reactor wall. The catalyst balance includes the heat associated with the reforming and water-gas-shift reactions, while the sorbent balance includes the heat released by carbonation. Gas-solid heat-transfer coefficients are evaluated from the correlations used in the integrated fluidised-bed model [18, 19].

The sorbent energy balance is

$$C_{solid}\left(T_s, Q\right)\frac{dT_s}{dz} = Q'_{gs} + A\,R_c\left[-\Delta H_{carb}\left(T_s\right) + h_{CO_2}\left(T_g\right) - h_{CO_2}\left(T_s\right)\right] + q'_{w,s} + q'_{e,s} \tag{17}$$

The catalytic and carbonation heat contributions are also accumulated directly during the axial solution. This provides consistent totals for the reaction-energy terms, particularly because the reforming reactions are strongly concentrated near the reactor inlet.

The coupled species and energy balances are solved simultaneously as a stiff axial initial-value problem. The solution tracks the gas-species molar flows, captured CO_2, gas temperature, catalyst temperature, sorbent temperature, and cumulative reaction-energy terms from the reactor inlet to the outlet.

At the reactor outlet, an algebraic calciner control volume closes total calcium, the calcium oxide and calcium carbonate flows, solids circulation, carbon dioxide release, and the calciner energy demand. The calciner is ideal and algebraic: its geometry, solids residence time, and calcination kinetics are not modelled. Its duty is decomposed into five reported channels, and the minimum requirement is their sum,

$$Q_{\min} = Q_{calcination} + Q_{sorbent,sens} + Q_{catalyst,sens} + Q_{CO_2,released} + Q_{declared\ gas} \tag{18}$$

with the external duty following as $Q_{ext} = Q_{\min}/\left(1 - f_{loss}\right)$.

2.8 The KU pilot-scale bubbling fluidised-bed model

2.8.1 Reactor scope and geometry

The third phase of the practicum developed a separate model for the Khalifa University (KU) pilot-scale bubbling fluidised-bed reactor. The physical KU system does not contain a riser, loop seal, continuous solids-return line, external carbonator, or calciner. It is therefore modelled as a bubbling fluidised-bed SER reactor with a finite catalyst and CaO inventory rather than as a continuous calcium-looping system. The gas phase is solved quasi-steadily at each sorbent state, while the average sorbent conversion is integrated continuously with time. This allows the model to resolve the gradual exhaustion of the finite CaO inventory and the resulting breakthrough behaviour.

The modelled reactor includes the gas inlet and distributor, the reacting bubbling bed containing nickel catalyst and CaO, the bubble and emulsion gas phases, the freeboard above the expanded bed, the transition section, and the disengagement section leading to the outlet and downstream filters. The filters are not represented as an intentional sorbent outlet because no experimental solids-loss data were available.

The supplied geometry is given in Table 5.

Table 5 Supplied geometry of the KU pilot-scale bubbling fluidised bed.

Section	Length	Internal diameter
Straight bed	32 in = 0.8128 m	2.00 in = 0.0508 m
Transition cone	3 in = 0.0762 m	2.00 in → 3.75 in
Disengagement	4 in = 0.1016 m	3.75 in = 0.09525 m

The supplied section dimensions sum to 39 in, while a 36 in heated length is reported separately. These quantities may refer to different physical extents; therefore, the exact heated region should be confirmed against the equipment documentation. The 39 in development

geometry is retained in the present model to preserve reproducibility of the reported simulations. The local cross-sectional area and superficial velocity follow

$$A(z) = \frac{\pi D(z)^2}{4}, \qquad U(z) = \frac{\dot{n}_{tot}(z)\, R\, T}{P\, A(z)} \tag{19}$$

Because the area expands by a factor of 3.5156 between the bed and the disengagement section, the superficial velocity falls by about 72% over that transition.

2.8.2 Bubbling-bed hydrodynamics

The hydrodynamic treatment follows standard bubbling-bed correlations. The Archimedes number is

$$Ar = \frac{\rho_g\, d_p^3\, (\rho_p - \rho_g)\, g}{\mu^2} \tag{20}$$

Minimum fluidisation follows Wen and Yu [17] in the form $Ar = 1650\, Re_{p,mf} + 24.5\, Re_{p,mf}^2$, from which u_{mf} follows through the particle Reynolds number. Terminal velocity uses the explicit Haider–Levenspiel form [20]

$$u_t = u_t^* \left[\frac{\mu\, (\rho_p - \rho_g)\, g}{\rho_g^2} \right]^{1/3}, \qquad u_t^* = \left[\frac{18}{Ar^{2/3}} + \frac{0.591}{Ar^{1/6}} \right]^{-1} \tag{21}$$

Bubble diameter increases with axial position according to the Darton correlation [21]:

$$d_b(z) = \frac{0.54\, (U - u_{mf})^{0.4}\, z^{0.8}}{g^{0.2}} \tag{22}$$

The bubble rise velocity is $u_{br} = 0.711\sqrt{g\, d_b}$, the absolute bubble velocity $u_b = (U - u_{mf}) + u_{br}$, the bubble holdup $\delta = (U - u_{mf})\,/u_b$, the emulsion solids volume fraction $\phi_{solid} = (1-\delta)\,(1 - \varepsilon_{mf})$ and the expanded bed height $H = H_{mf}/(1 - \delta)$. Slugging is screened against the criterion $d_b > \frac{2}{3} D_{bed}$, while the ratio U/u_t is used as an entrainment/transport diagnostic. These relations provide operating regime checks rather than a detailed prediction of particle entrainment or loss.

2.8.3 Bubble–emulsion gas exchange and species balances

Gas in the bubbles contacts almost no solids, so the two phases are tracked separately and exchange gas through the Kunii–Levenspiel interchange coefficients, evaluated per species because the diffusivities differ substantially [15]:

$$K_{bc,i} = 4.5 \frac{u_{mf}}{d_b} + 5.85 \frac{D_i^{0.5} g^{0.25}}{d_b^{1.25}}, \qquad K_{ce,i} = 6.77 \left(\frac{\varepsilon_{mf} D_i u_b}{d_b^3} \right)^{1/2} \tag{23}$$

combined in series as $1/K_{be,i} = 1/K_{bc,i} + 1/K_{ce,i}$. All three coefficients have units of s^{-1} and are defined per unit bubble volume, so the reactor-volume transfer term requires only the bubble holdup and no interfacial-area factor [15]:

$$R_{be,i} = \delta\, K_{be,i}\, (C_{b,i} - C_{e,i}) \tag{24}$$

Species diffusivities in the mixture use Fuller binaries [12] combined by the Wilke–Blanc rule. The integrated states are the species molar flows in each phase, and the balances are

$$\frac{dF_{b,i}}{dz} = -A\,R_{be,i} + q_i, \qquad \frac{dF_{e,i}}{dz} = +A\,R_{be,i} - q_i + A\,R_{rxn,i} \tag{25}$$

with the sign convention that $R_{be,i}$ leaves the bubble and enters the emulsion, and that $R_{rxn,i}$ appears only in the emulsion because all heterogeneous reaction is allocated to the emulsion solids.

Reforming increases the number of gas moles, so the total molar flow and the superficial velocity rise along the bed. That reaction-generated gas is repartitioned by a hydrodynamic crossflow q_i, kept explicitly separate from the diffusive exchange. Requiring the Kunii–Levenspiel condition $U_e = u_{mf}$, and noting that the total species flows obey $dF_i/dz = A\,R_{rxn,i}$ independently of both R_{be} and q, gives

$$Q_{cross} = A\sum_i R_{be,i} + A\sum_i R_{rxn,i} - \frac{dG}{dz}, \qquad G(z) = \frac{A\,u_{mf}\,P}{R\,T} \tag{26}$$

with $q_i = Q_{cross}\,x_{donor,i}$ and the transported composition upwinded. Elements are conserved because the crossflow components sum to Q_{cross} and enter the two phases with opposite signs.

2.8.4 Reforming chemistry and CaO carbonation

The KU model retains the same methane reforming chemistry established during the fixed-bed phase. Steam methane reforming, global reforming, and water-gas-shift rates follow the Xu–Froment kinetic formulation [3], with the Twigg equilibrium relationships [4]. Unlike the fixed-bed DAE model, the present reduced-order KU formulation evaluates the catalytic rates using the bulk emulsion composition and does not include a separate catalyst-film calculation.

Carbon dioxide capture occurs through

$$\mathrm{CaO} + \mathrm{CO_2} \rightleftharpoons \mathrm{CaCO_3} \tag{27}$$

and the carbonation treatment is inherited from the parent SER formulation [1, 2, 6]. The carbonation rate decreases as the sorbent approaches its available fast-stage capacity. The baseline inherited parameters are the maximum conversion $X_{\max} = 0.4$ and the carbonation rate constant $k_{\mathrm{carb}} = 0.35\ \mathrm{s}^{-1}$. These values are inherited material-model parameters rather than measured properties of the KU sorbent. The equilibrium CO_2 pressure is evaluated from the Baker relationship [7]. The fast-stage capacity treatment is consistent with the established SER formulation and with the distinction between the initial kinetically controlled carbonation regime and the much slower product-layer-diffusion regime [6].

The solid loading is represented using a baseline sorbent-to-catalyst volume ratio of 5:1 inherited from the fixed-bed SER formulation [1, 2]. This ratio is not claimed to represent the final experimental KU loading and can be replaced once the actual catalyst and sorbent inventory is specified.

2.8.5 Transient well-mixed sorbent model

The principal dynamic state of the KU model is the population-average CaO conversion X. The catalyst and sorbent remain physically discrete particles, but strong bubbling-bed solids mixing is represented by a single well-mixed average sorbent state rather than an axial sorbent-conversion profile.

At each value of X, the bubble-emulsion gas equations are solved to quasi-steady state. The resulting total reactor carbonation rate is then used to advance the sorbent conversion in time. The transient therefore operates as

$$X(t) \longrightarrow \text{quasi-steady gas-phase model} \longrightarrow \dot{n}_{CO_2,captured} \longrightarrow \frac{dX}{dt}$$

The overall sorbent conversion rate is obtained from the captured CO_2 rate and the available CaO inventory:

$$\frac{dX}{dt} = \frac{\dot{n}_{CO_2,captured}}{n_{CaO,0}} \qquad \text{for } 0 \leq X \leq X_{max} \tag{28}$$

Here, $n_{CaO,0}$ is the initial number of moles of CaO available for carbonation. The value $X_{max} = 0.4$ is the fast-stage conversion limit inherited from the reference SER formulation [1, 2]. It is a provisional material-model parameter for the present KU model rather than a measured property of the KU sorbent and should be replaced by experimentally determined capacity when those data become available.

This treatment exploits the separation between the relatively fast gas-phase response and the much slower exhaustion of the solid inventory. It therefore resolves the complete sorbent-capacity trajectory without requiring a fully transient multiphase CFD calculation. The model predicts an extended pre-breakthrough period followed by a rapid decline in capture and SER performance as it approaches its maximum available capacity.

2.8.6 Thermal treatment

The physical KU column is externally heated, and the nominal operating temperature used in the present work is 873.15 K. The heated case is therefore used as the principal representation of the actual reactor. Isothermal and adiabatic calculations are retained only as limiting thermal-boundary comparisons.

The reactor energy accounting includes the endothermic reforming heat, the exothermic carbonation heat, the sensible energy change, and any external heat supplied through the reactor boundary. The overall first-law balance may be expressed as

$$Q_{ext} = Q_{reforming} - Q_{carbonation} + \Delta H_{sensible} \tag{29}$$

with the sign convention defined consistently in the model.

The heated boundary condition supplies the external heat required to maintain the selected reactor temperature. When the heated and isothermal calculations are constrained to the same bed temperature, they produce the same chemistry; the difference lies only in how the thermal boundary condition is represented. In contrast, the adiabatic reactor receives no external heat, and its temperature changes in response to the competing heat effects of reforming and carbonation.

2.9 Numerical verification across the three models

Verification was treated as a standing requirement rather than a closing step, and in every case it is numerical verification, not experimental validation.

For the fixed-bed models, each accepted case was checked for elemental closure in carbon, hydrogen, and oxygen, and for the absence of numerical damage. The thermodynamic layer carries its own regression suite, and the methane NASA-7 coefficients are guarded digit-exact against GRI-Mech 3.0.

For the circulating fluidised-bed model, every completed case is subjected to carbon, hydrogen, oxygen, calcium, and total-solids balances; to reactor, calciner, and complete loop-energy balances; to solver-tolerance and axial-grid sensitivity; to hydrodynamic regime and transport-margin checks; and to reproducibility checks. A case is accepted only when the required numerical, physical, and conservation tolerances are all satisfied.

3 Results

3.1 Final fixed-bed benchmark at the reference grid

The results in this section are the completed model-to-model benchmark, performed at the reference resolution of 140 axial nodes for both implementations. They are not compared with experimental measurements at any point.

Before the integral indicators, it is worth looking at what the models actually compute. Figure 2 shows the axial state of the bed part-way through a run: the gas temperature field, the species mole fractions, the hydrogen profile and the two reaction-rate profiles. The structure visible there is the physical signature of sorption-enhanced reforming. Methane is consumed within the first metre or so, where the endothermic reforming produces a sharp inlet temperature depression, while the carbonation source is displaced further along the bed and releases heat where the reforming has already slowed. The two rate profiles do not overlap; they are staggered, and the gas phase is what thermally connects them.

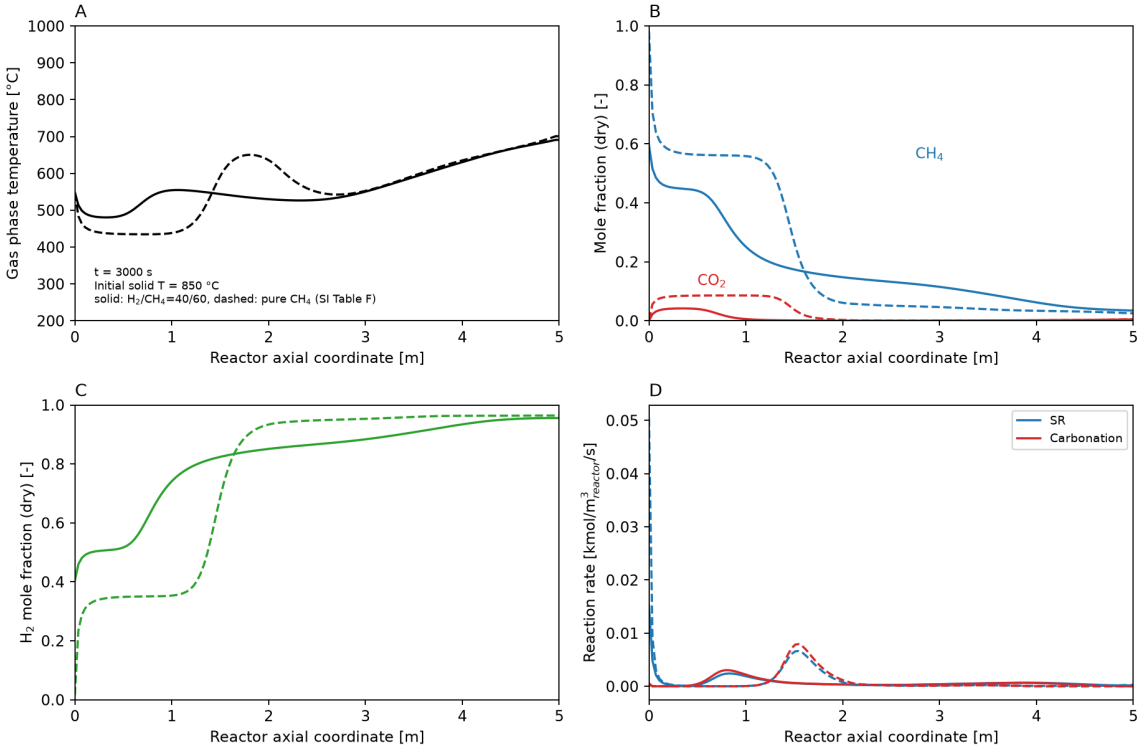


Figure 2 Axial state of the fixed bed at $t = 3000$ s, computed by the DAE implementation at the $N = 140$ reference grid: (A) gas temperature, (B) dry mole fractions of CH_4 and CO_2, (C) hydrogen mole fraction, (D) steam-reforming and carbonation rate profiles. Solid lines are the 40/60 H_2/CH_4 feed and dashed lines pure CH_4, following the line mapping of the reference Supporting Information.

The transient behaviour that those profiles eventually produce is shown in Figure 3. Each case holds a long high-conversion, hydrogen-rich plateau while the sorbent still has available capacity, and then passes through breakthrough as the carbonation front reaches the bed exit: the outlet CO_2 fraction rises sharply, methane conversion and hydrogen content fall to their unenhanced values, and the outlet temperature settles onto a lower plateau once the carbonation exotherm is no longer available. Increasing the hydrogen content of the feed delays breakthrough, because less methane is converted per unit time and the sorbent is therefore consumed more slowly.

Table 6 gives the ODE benchmark at the reference grid and Table 7 the DAE benchmark. In

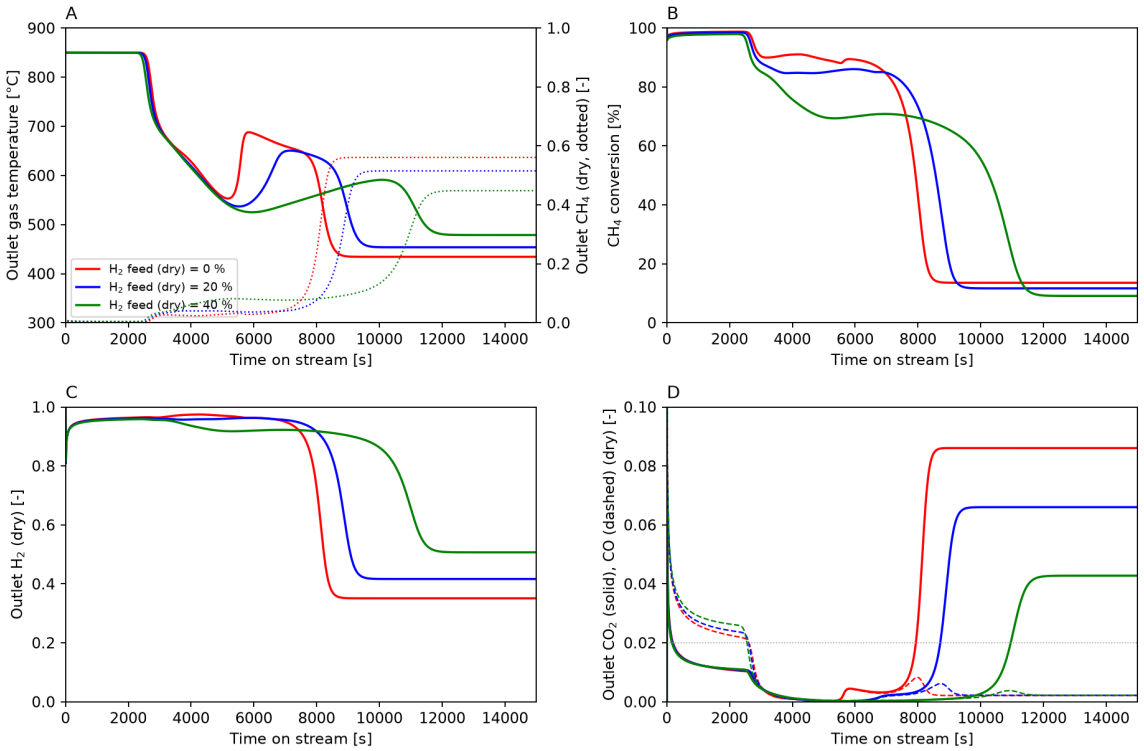


Figure 3 Effect of hydrogen content in the feed on the outlet transients at the $N = 140$ reference grid, for $P = 10$ bar, $S/C = 4$, $T_f = 550$ °C and $T_{bed} = 850$ °C: (A) outlet gas temperature with the dry outlet CH_4 fraction dotted, (B) methane conversion, (C) dry hydrogen fraction, (D) dry outlet CO_2 (solid) and CO (dashed). The dotted horizontal line in (D) marks the 0.02 breakthrough criterion.

both tables, the model and reference columns are the reported values; the difference column has been recomputed from those two columns. Values marked with an approximate sign were read from figures in the reference work rather than from tabulated numbers, and their differences are correspondingly approximate.

Table 6 Final ODE benchmark against the reference model at $N = 140$. The carbon capture ratio and breakthrough time for the propane case are taken from the model's output, as quoted in the source report discussion, rather than from its main comparison table.

Case	KPI	ODE	Reference	Difference
Pure CH_4	CH_4 conversion	90.2%	91.5%	−1.3 pp
	Net H_2 yield	89.0%	89.5%	−0.5 pp
	H_2 purity (dry)	95.6%	95.9%	−0.3 pp
	CCR	83.6%	84.6%	−1.0 pp
	BTt	8027 s	≈ 8000 s	≈ +27 s
20/80 H_2/CH_4	CH_4 conversion	86.0%	≈ 87.0%	≈ −1.0 pp
	Net H_2 yield	84.8%	≈ 85.5%	≈ −0.7 pp
	H_2 purity (dry)	94.7%	≈ 95.0%	≈ −0.3 pp
	CCR	79.7%	≈ 81.0%	≈ −1.3 pp
40/60 H_2/CH_4	CH_4 conversion	74.1%	74.4%	−0.3 pp
	Net H_2 yield	73.0%	73.0%	0.0 pp
	H_2 purity (dry)	91.9%	92.1%	−0.2 pp
	CCR	68.6%	69.2%	−0.6 pp
40/60, $\xi_{inert} = 0.34$	CH_4 conversion	93.7%	93.4%	+0.3 pp
	Net H_2 yield	90.4%	≈ 90.0%	≈ +0.4 pp
	H_2 purity (dry)	94.7%	≈ 95.0%	≈ −0.3 pp
	CCR	76.1%	77.7%	−1.6 pp
40/45/15 $H_2/CH_4/C_3H_8$	Hydrocarbon conversion	93.5%	92.8%	+0.7 pp
	Net H_2 yield	90.3%	89.2%	+1.1 pp
	H_2 purity (dry)	94.6%	95.6%	−1.0 pp
	CCR	78.7%	82.6%	−3.9 pp
	BTt	8629 s	not reported	–

Table 7 Final DAE benchmark against the reference model at $N = 140$. This is the authoritative final fixed-bed result set of the practicum.

Case	KPI	DAE	Reference	Difference
Pure CH_4	CH_4 conversion	90.67%	91.5%	−0.83 pp
	Net H_2 yield	89.45%	89.5%	−0.05 pp
	H_2 purity (dry)	95.65%	95.9%	−0.25 pp
	CCR	83.71%	84.6%	−0.89 pp
	BTt	7934 s	≈ 8000 s	≈ −66 s
20/80 H_2/CH_4	CH_4 conversion	86.9%	≈ 87.0%	≈ −0.1 pp
	Net H_2 yield	85.7%	≈ 85.5%	≈ +0.2 pp
	H_2 purity (dry)	94.9%	≈ 95.0%	≈ −0.1 pp
	CCR	80.3%	≈ 81.0%	≈ −0.7 pp
40/60 H_2/CH_4	CH_4 conversion	75.1%	74.4%	+0.7 pp
	Net H_2 yield	74.0%	73.0%	+1.0 pp
	H_2 purity (dry)	92.2%	92.1%	+0.1 pp
	CCR	69.2%	69.2%	0.0 pp
	BTt	10956 s	≈ 11500 s	≈ −544 s
40/60, $\xi_{inert} = 0.34$	CH_4 conversion	93.4%	93.4%	0.0 pp
	Net H_2 yield	90.2%	≈ 90.0%	≈ +0.2 pp
	H_2 purity (dry)	94.6%	≈ 95.0%	≈ −0.4 pp
	CCR	75.5%	77.7%	−2.2 pp
40/45/15 $H_2/CH_4/C_3H_8$	Hydrocarbon conversion	93.36%	92.8%	+0.56 pp
	Net H_2 yield	90.22%	89.2%	+1.02 pp
	H_2 purity (dry)	94.48%	95.6%	−1.12 pp
	CCR	78.07%	82.6%	−4.53 pp
	BTt	8625 s	not reported	–

The summary of these two tables is that most conversion, hydrogen-yield, and purity values are reproduced closely, generally within about one percentage point, while some carbon-capture metrics show larger deviations in selected cases. It would be wrong to claim that everything agrees within one per cent. For the pure-methane DAE case, the net hydrogen yield differs by

0.05 percentage points, purity by 0.25, and the capture ratio by 0.89, which is close agreement by any reasonable standard. At the other extreme, the carbon capture ratio of the 15% propane case deviates by 4.53 percentage points in the DAE and by approximately 3.9 percentage points in the ODE. That deviation is the largest in the whole benchmark; it appears consistently in both independent implementations, and it is discussed further in subsection 4.2.

Figure 4 shows how the integral indicators respond to hydrogen in the feed, with the reference values marked. Both models reproduce the inhibition mechanism: increasing the dry hydrogen fraction to 40% reduces methane conversion, hydrogen yield, and carbon capture, because hydrogen suppresses both reforming and the shift and therefore also reduces the heat released in the moving carbonation zone. The reference points lie close to the computed curves over the entire range, and the trend in the uncaptured-carbon distribution indicates that the loss is dominated by unconverted methane rather than by carbon monoxide slip.

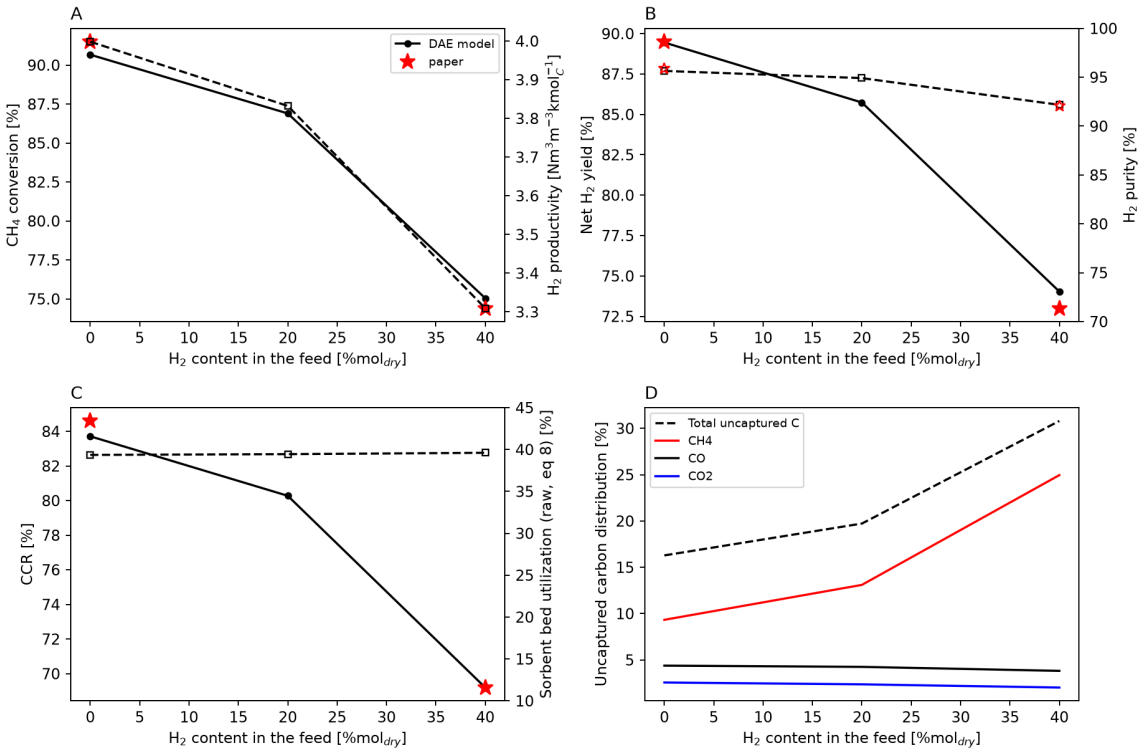


Figure 4 Integral performance indicators as a function of hydrogen content in the feed, computed by the DAE implementation at the $N = 140$ reference grid, with the published reference values overlaid as red stars: (A) methane conversion and hydrogen productivity, (B) net hydrogen yield and purity, (C) carbon capture ratio and raw sorbent bed utilisation, (D) distribution of uncaptured carbon between CH_4, CO and CO_2.

Both models also reproduce the effect of an inert heat carrier. Replacing part of the sorbent with dense alumina pellets increases the bed's thermal capacity and maintains a higher temperature through the reforming zone; for the 40/60 hydrogen-methane feed, methane conversion rises from roughly 74% to roughly 93%. The trade-off is visible directly in Figure 5: the reduced sorbent inventory brings breakthrough earlier, so the high-conversion plateau is shorter at $\xi_{inert} = 0.34$ than at $\xi_{inert} = 0$, thereby increasing the number of reforming-regeneration cycles required.

Figure 6 places the final DAE results against thermodynamic equilibrium at the same pressure. Reading the categories as defined in the reference work, Mix 1 is the 40/60 H_2/CH_4 feed and Mix 2 the 40/45/15 $H_2/CH_4/C_3H_8$ feed, both on a dry molar basis. The adiabatic fixed-bed

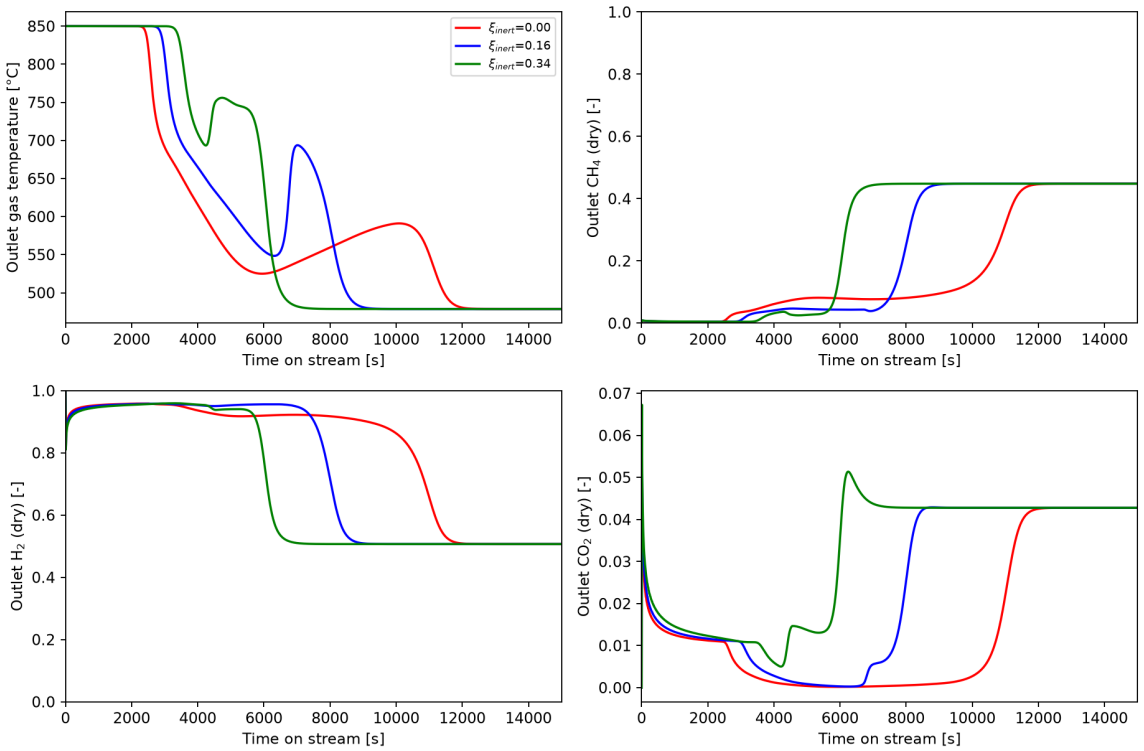


Figure 5 Effect of the inert heat-carrier volume fraction ξ_{inert} on the outlet transients for the 40/60 H_2/CH_4 feed at the $N = 140$ reference grid: outlet gas temperature, dry outlet CH_4, dry outlet H_2 and dry outlet CO_2. Raising ξ_{inert} sustains a higher reforming temperature but shortens the pre-breakthrough period.

results sit between the 600 and 700 °C equilibrium bounds for most indicators, which is the expected position for a bed whose reforming zone operates below the initial solids temperature. For Mix 1, adding the inert heat carrier at $\xi_{inert} = 0.34$ lifts conversion and yield above both equilibrium bounds, consistent with the higher sustained reforming temperature reported above.

Together, Figures 2–6 and Tables 6–7 complete the fixed-bed Phase I result set. The next subsection begins the physically separate circulating-fluidised-bed study.

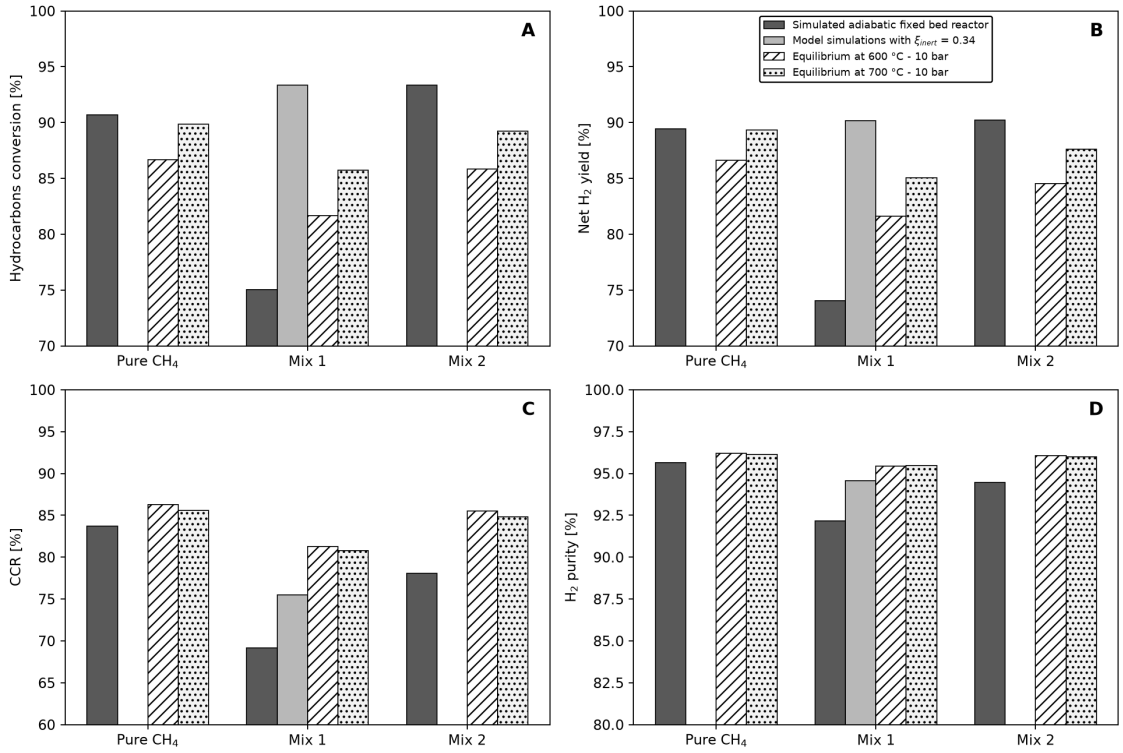


Figure 6 Final DAE fixed-bed results compared with the inert-carrier case and with thermodynamic equilibrium at 600 and 700 °C, all at 10 bar: (A) hydrocarbon conversion, (B) net hydrogen yield, (C) carbon capture ratio, (D) hydrogen purity. Mix 1 is 40/60 H_2/CH_4; Mix 2 is 40/45/15 $H_2/CH_4/C_3H_8$ (%mol, dry). The $\xi_{inert} = 0.34$ series was run for Mix 1 only.

3.2 Circulating fluidised-bed (SER-CFB) results

This subsection reports the steady-state circulating fluidised-bed results. The comparison is deliberately controlled: the **Initial case** is the baseline, and the **Final case** differs only by a 50% increase in static solids inventory. Solids circulation, reactor geometry, feed, steam-to-carbon ratio, reaction and equilibrium relations, transport and heat-transfer closures, and solver settings are unchanged. "Final case" here means the selected reference case for the present reduced-order model; it is not an experimentally demonstrated optimum.

3.2.1 Controlled solids-inventory comparison

The hypothesis was that extending the solids-rich contact region, without increasing the circulation of regenerated sorbent, would allow more of the carbon dioxide generated further along the riser to meet sorbent. Testing required a controlled change, so the static solids inventory was increased by 50%, and nothing else was altered. The solids circulation rate, reactor geometry, methane feed, steam-to-carbon ratio, kinetic expressions, equilibrium relations, contact and transport correlations, heat-transfer treatment, and solver tolerances were all held unchanged. The inventory multiplier was the only operating input modified. The dense-zone height is not prescribed directly; it follows from the solids-inventory closure. Increasing the static inventory therefore extends the solids-rich lower region and changes gas-solid contact without changing the rate at which regenerated sorbent is circulated through the loop.

Figure 7 shows the effect on the axial solids distribution. The dense zone lengthens from 3.09 to 7.10 m, and the lean-zone profile above it sits at a higher solids fraction over the following ten to fifteen metres before both cases relax to the same asymptote. Figure 8 shows the consequence

for capture: the carbonation-rate profile retains a significant second contribution around the extended dense-zone boundary, and the cumulative captured-carbon curve separates from the initial case and stays separated to the top of the riser.

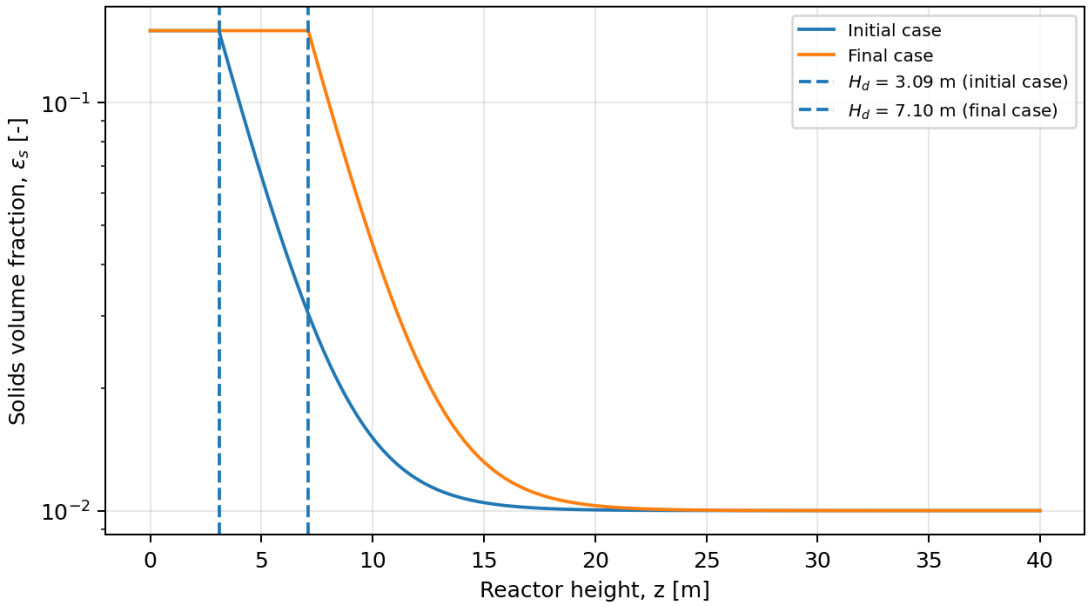


Figure 7 Axial solids-fraction profiles for the initial case and for the final case, with the calculated dense-zone height marked for each. Increasing the static inventory by 50% extends the dense zone from 3.09 to 7.10 m and raises the solids fraction.

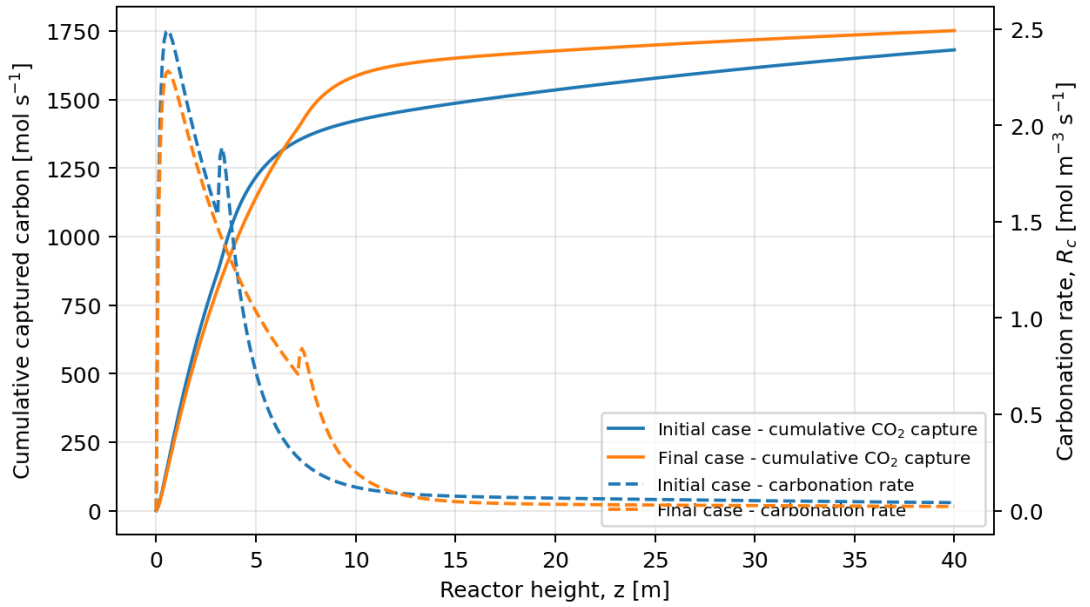


Figure 8 Carbonation rate and cumulative captured carbon along the riser for the initial case and for the final case. The extended contact region sustains carbonation further along the riser, and the cumulative capture curves separate and remain separated.

Two carbon-capture metrics are reported because they answer different questions. The CO_2 capture efficiency is the captured CO_2 divided by captured plus outlet CO_2; it measures how

Table 8 Initial case compared with the final case. Only the static solids inventory was changed between them.

Quantity	Initial case	Final case	Change	Unit
Total solids inventory	283 103.2	424 654.8	+141 551.6	kg
Dense-zone height H_d	3.0891	7.1039	+4.0148	m
CH_4 conversion	95.6047	95.9846	+0.3799	percentage points
Normalised H_2 yield	92.5716	93.1922	+0.6206	percentage points
Dry H_2 purity	92.2295	92.9384	+0.7089	percentage points
CO_2 capture	82.4259	84.5091	+2.0832	percentage points
Carbon capture ratio	68.8029	71.6764	+2.8735	percentage points
H_2 production	18.2362	18.3585	+0.1223	kg s^{-1}
Thermal loop duty	11.6830	11.6717	−0.0113	kWh_{th} kg^{-1} H_2
Pressure drop	19.837	29.756	+9.919	kPa

effectively the carbon dioxide that is formed is removed. The carbon capture ratio (CCR) is the captured carbon divided by the total carbon fed as methane. CCR is therefore lower because carbon that leaves as unconverted CH_4 or CO is also counted against the feed-carbon denominator.

The principal result is the carbon capture ratio, which increases from 68.8029% to 71.6764%. Conversion, yield, purity, and hydrogen production all improve simultaneously but modestly. The specific reactor-calciner thermal duty is essentially unchanged, moving from 11.6830 to 11.6717 kWh_{th} per kilogram of hydrogen, and the reason is straightforward: the additional hold-up is static, and no additional regenerated solids are being circulated, so the calciner duty per unit of hydrogen barely moves. The penalty is hydrodynamic. Pressure drop increases by half, from 19.8 to 29.8 kPa, and the system must hold 50% more solids. Figure 9 makes that trade-off visible along the riser: the cumulative pressure-drop profile separates strongly between the two cases, while the gas-temperature profiles retain the same overall structure and differ by only a few kelvin over most of the upper riser. The reported reactor-calciner duty is a thermal quantity and does not include blower power or other electrical costs associated with the larger pressure drop; an essentially unchanged kWh_{th} kg^{-1} H_2 therefore does not mean the Final case is cost-free at plant level.

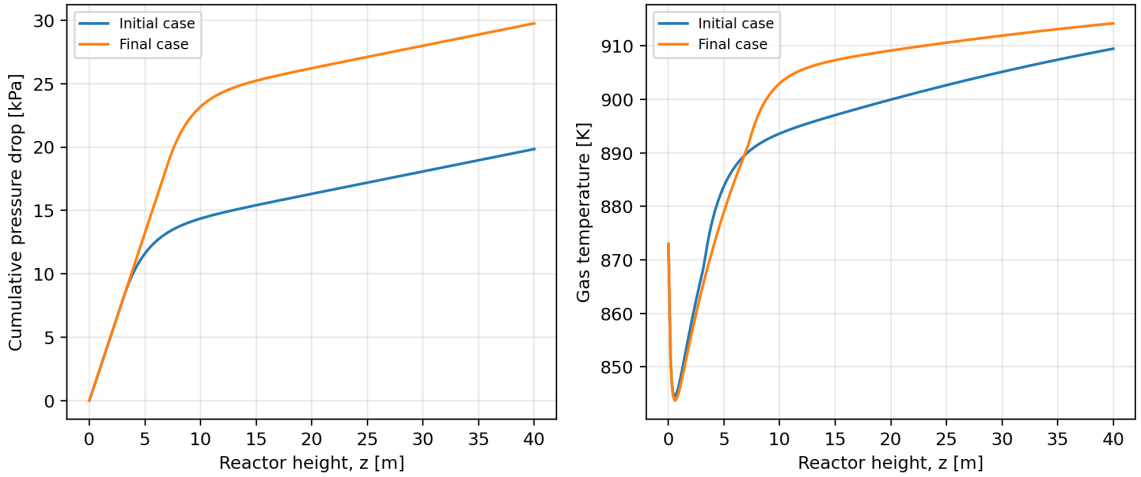


Figure 9 Hydrodynamic and thermal response of the initial and final SER-CFB cases: (left) cumulative pressure drop and (right) gas temperature along the 40 m riser. Increasing static solids inventory raises the pressure-drop penalty substantially, while the overall gas-temperature profile changes more modestly.

Carbon, hydrogen, oxygen, calcium, solids, and energy balances satisfied the numerical closure criteria for the final case.

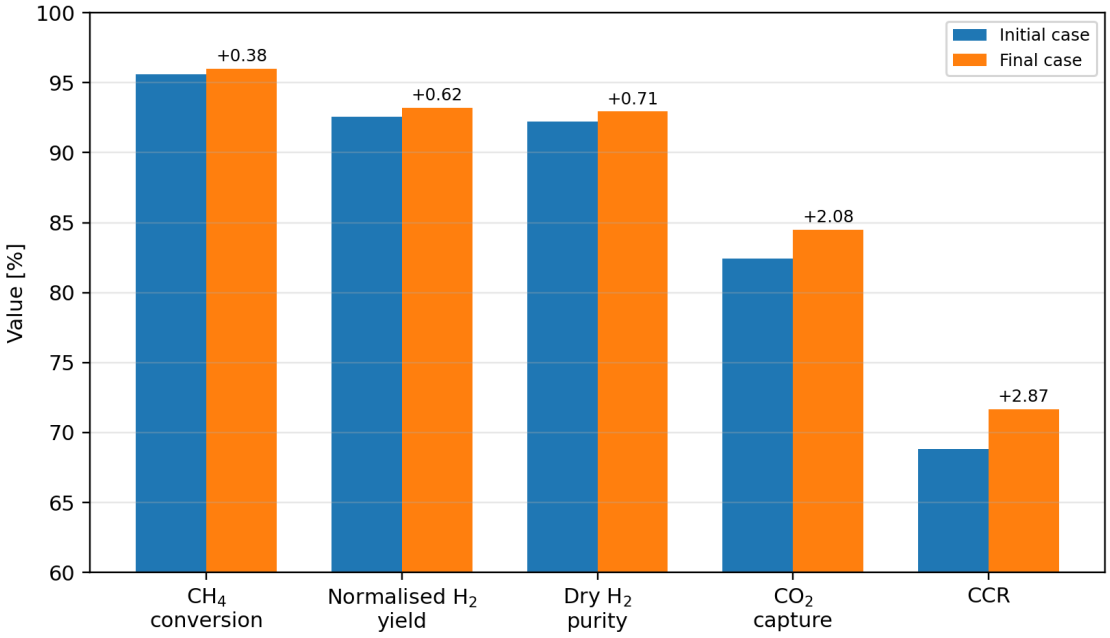


Figure 10 Key performance indicators for the initial case and the final case. Conversion, yield, and purity improve modestly, while the carbon capture ratio improves by 2.87 percentage points.

The SER-CFB results should be interpreted as large-scale model-development results rather than predictions for a specific existing reactor. No dedicated CFB reactor geometry was available for this phase of the practicum; consequently, the riser geometry and hydrodynamic structure were based on the Romano carbonator framework [14]. The resulting reactor and gas-flow basis are on an industrial scale, which explains the comparatively large predicted hydrogen production. Absolute quantities such as hydrogen production and solids inventory are therefore strongly dependent on the adopted geometry and operating scale and should not be interpreted as design values for the KU pilot reactor or another specific facility. The principal value of the present CFB model is instead in examining the effects of variables such as solids inventory, solids distribution, circulation, reaction coupling, and carbon capture within a consistent reduced-order framework.

3.3 KU pilot-scale bubbling fluidised-bed (BFB) results

The third model concerns the KU pilot rig. The results are grouped below into hydrodynamics, fresh-sorbent and breakthrough behaviour, reactor energy and throughput effects, and the independent model-to-model benchmark.

3.3.1 Hydrodynamic baseline

Figure 11 shows the modelled geometry and the resulting cross-sectional area profile, including the expansion through the transition cone. As noted in subsubsection 2.8.1, the supplied section dimensions sum to 39 in while a 36 in heated length is reported separately; the 39 in development geometry is retained so that existing results remain reproducible, and the exact heated extent should be confirmed against the equipment documentation.

Table 9 gives the authoritative hydrodynamic baseline, evaluated on the reacting methane-steam mixture at the SER condition of 873.15 K. Every number, figure, and result file in this phase of the work uses this single baseline.

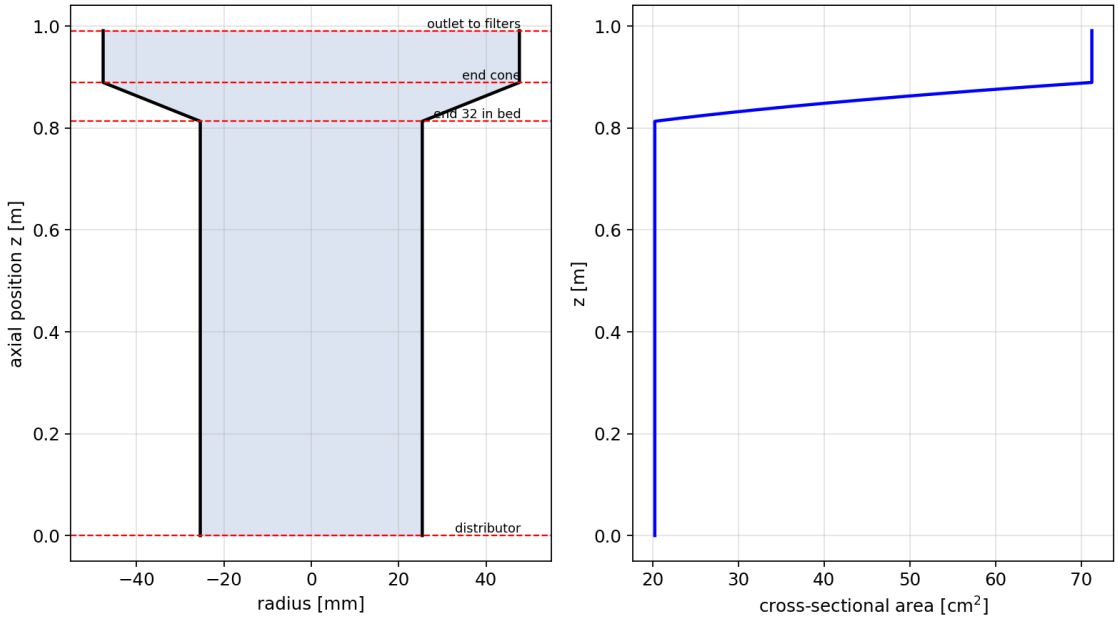


Figure 11 Modelled KU bubbling-bed reactor geometry and cross-sectional area profile. The development geometry retains the 39 in section sum; the separately reported 36 in heated length may refer to a different physical extent and requires equipment confirmation.

Table 9 Authoritative KU hydrodynamic baseline at the reacting SER condition of 873.15 K. Two superseded development states exist in the archived history and are not mixed with these values.

Quantity	Value
Gas density ρ_g	0.245932 kg m^{-3}
Gas viscosity μ_g	2.086106×10^{-5} Pa s
Archimedes number Ar	31.0236
Particle Reynolds number at u_{mf}	0.0187969
Minimum fluidisation velocity u_{mf}	0.0106296 m s^{-1}
Terminal velocity u_t	0.823968 m s^{-1}
Geldart classification	Group B
Superficial velocity at $3u_{mf}$	0.0318888 m s^{-1}
Expanded bed height H	0.220645 m
Bubble diameter d_b	0.0218356 m
Bubble holdup δ	0.0606838
Bubble-emulsion interchange K_{be}	6.92027 s^{-1}
Velocity ratio U/u_t	0.0387016
Fraction of the slugging limit at $3u_{mf}$	0.64

Figure 12 places the operating range against the characteristic velocities. The operating superficial velocity sits between one and two orders of magnitude below the terminal velocity across the whole range examined, so entrainment is not the binding constraint. Figure 13 shows what is: bubble diameter grows with velocity and crosses the two-thirds bed-diameter slugging screen between five and eight times minimum fluidisation, while the bubble-emulsion interchange coefficient falls monotonically as bubbles grow, because larger bubbles present less exchange area per unit volume.

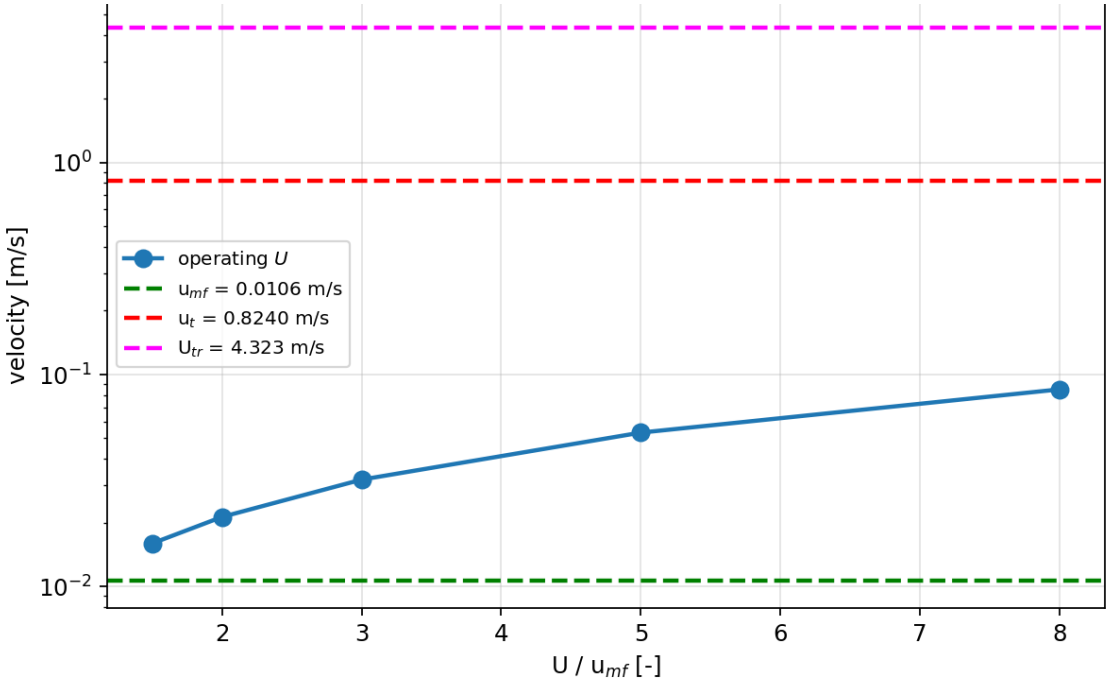


Figure 12 Fluidisation velocities at the reacting SER condition, showing the operating superficial velocity against the minimum fluidisation velocity, the terminal velocity and the transport velocity. Entrainment is not the binding constraint over the range examined.

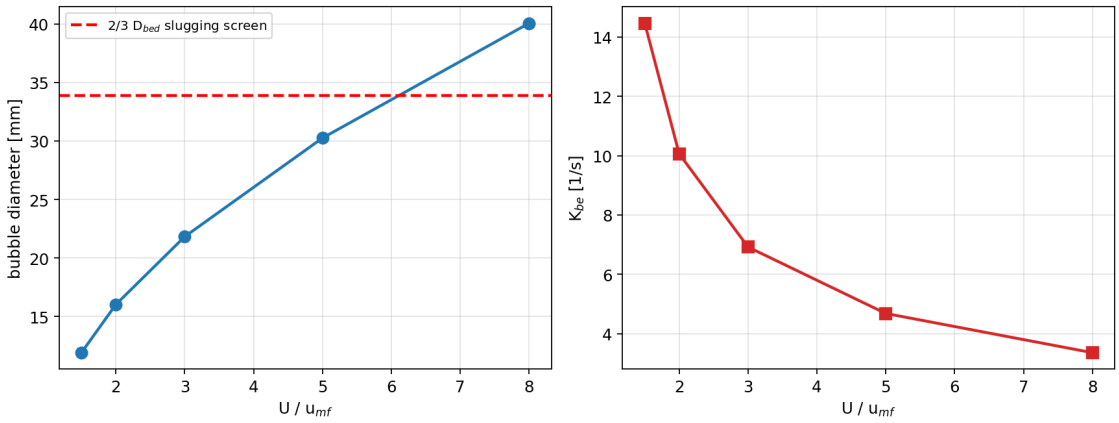


Figure 13 Bubble growth against the slugging screen (left) and the bubble-emulsion interchange coefficient (right) as functions of the velocity ratio. Bubble diameter crosses the two-thirds bed-diameter screen between five and eight times minimum fluidisation.

Both quantities in Figure 13 rest on a bubble-size prediction that is a lower bound, because the distributor geometry is unavailable and the porous-plate limit of the Darton correlation was used.

Real slugging would therefore be expected to appear earlier than the screen indicates, which is the conservative direction for a screening calculation but should not be mistaken for a margin.

3.3.2 Fresh-sorbent performance and capacity exhaustion

At the nominal heated operating point of 873.15 K and three times minimum fluidisation, the resolved trajectory has a pre-breakthrough dry hydrogen purity of 98.419%, methane conversion of 97.763% and carbon dioxide capture of 97.806%. These values describe the active-sorbent plateau of the current finite-inventory KU model; they should not be compared directly with the continuous CFB results as if the two reactor architectures had the same operating boundary.

The defining transient behaviour is exhaustion of the finite, well-mixed CaO inventory. In the heated 873.15 K case, breakthrough begins at 213.220 min, reaches its midpoint at 215.668 min, and is complete at 217.461 min, corresponding to sorbent conversions of 0.395817, 0.399273, and 0.399948. The transition lasts only 4.24 min and occupies the final ~1% of the available sorbent capacity.

Table 10 Resolved KU capacity-exhaustion trajectory at the nominal heated 873.15 K operating condition.

Quantity	Pre-breakthrough	Breakthrough transition	Post-breakthrough
Time [min]	0 – 213.22	213.22 – 217.46	217.46 – 290.8
Sorbent conversion X [–]	0 – 0.39582	0.39582 – 0.39995	→ 0.400
Dry H_2 purity [%]	98.419	98.419 → 75.000	75.000
CH_4 conversion [%]	97.763	97.763 → 80.758	80.758
CO_2 capture [%]	97.806	97.806 → 0.206	0.206

Figure 14 and Figure 15 show the resolved transition directly as a function of physical time. Reactor performance remains essentially constant for more than 213 min and then changes sharply as X approaches $X_{max} = 0.4$. The collapse is therefore an end-of-run capacity limit of a well-mixed sorbent inventory rather than propagation of a fixed-bed carbonation front.

3.3.3 Energy balance and superficial-velocity effects

The KU energy accounting covers the reactor only. There is no calciner duty, no sweep-gas heating, no sorbent circulation duty, no solids heat recovery and no whole-loop normalisation anywhere in this model, because none of that hardware exists in the current rig.

Table 11 and Figure 16 compare the three thermal boundary conditions at the same 873.15 K reference temperature.

At 873.15 K, the isothermal and heated cases are chemically identical: both give the same conversion, purity, and capture because the bed temperature is the same. The difference is only how 4.144 W of external heat is supplied; in the heated representation, the wall is 875.503 K. This 4.144 W is the external reactor duty of the fresh-sorbent thermal-boundary comparison, and it is therefore not the same quantity as the heater duty reported at each throughput in the velocity study below. The adiabatic case supplies no external duty and therefore cannot hold the set point, settling at 809.349 K. The interpretation is that the selected operating temperature matters, whereas the mathematical labels ‘heated’ and ‘isothermal’ do not change the chemistry when both maintain the same bed temperature.

The velocity study, reported in Table 12 and Figure 17, uses the heated 873.15 K operating condition and resolves the full sorbent trajectory at each throughput. The heater duties listed there are the duties required at each velocity; at $3u_{mf}$ the value is 3.968 W.

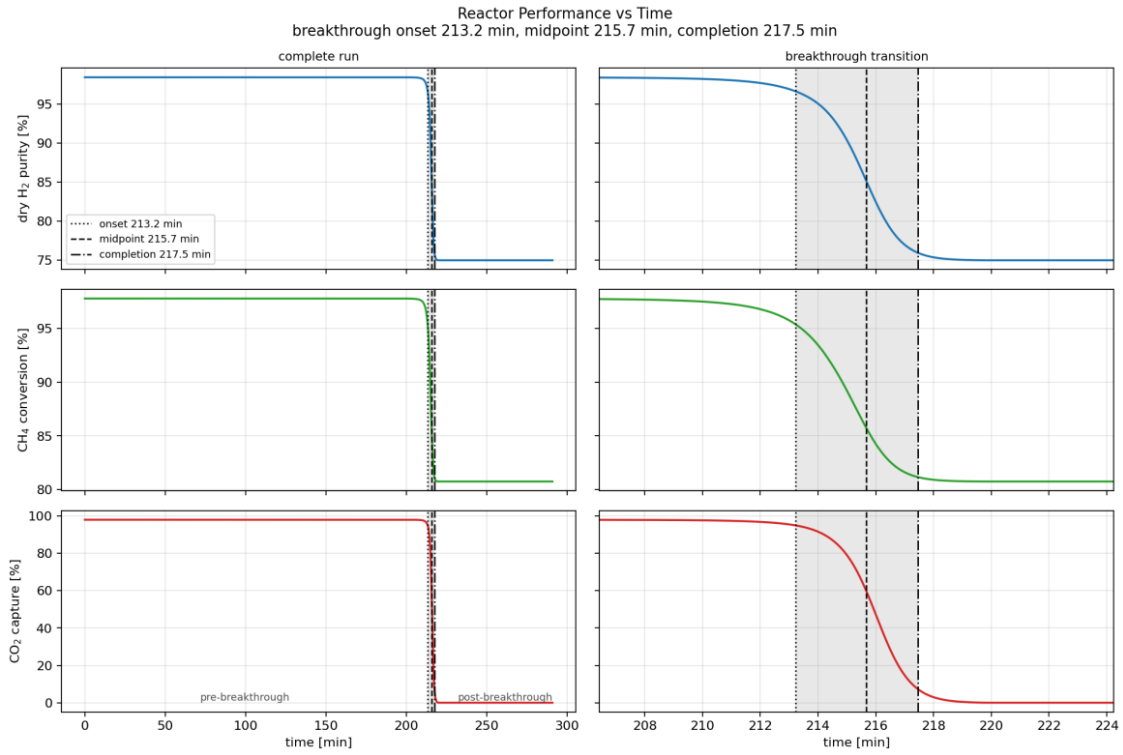


Figure 14 KU reactor performance versus time at the 873.15 K operating condition, showing breakthrough onset, midpoint and completion.

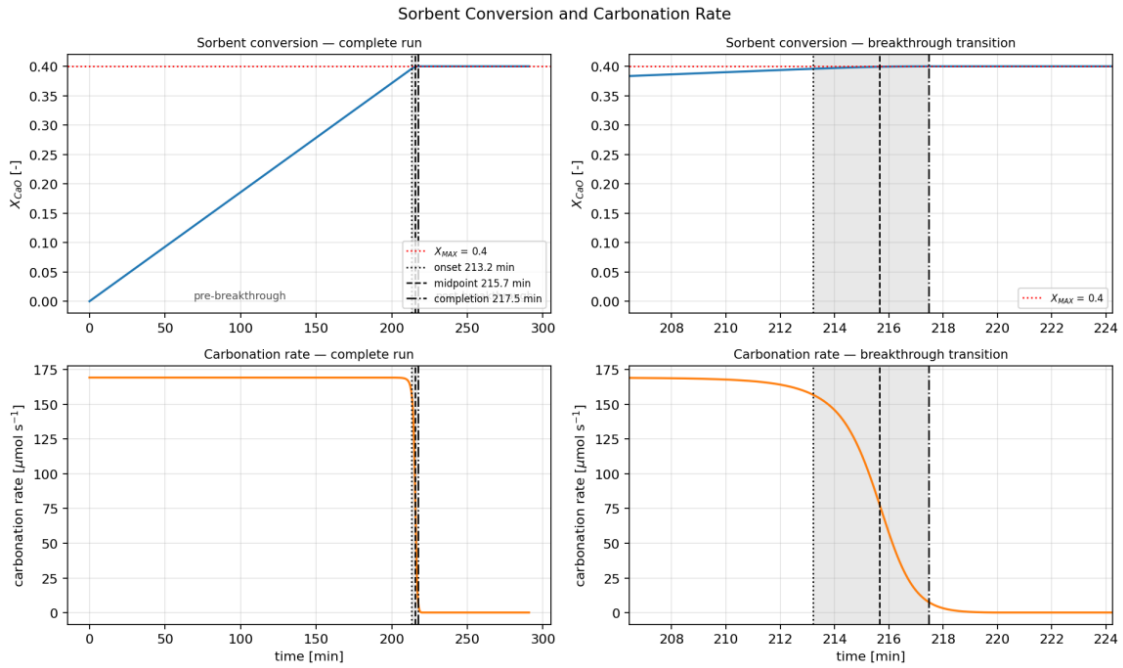
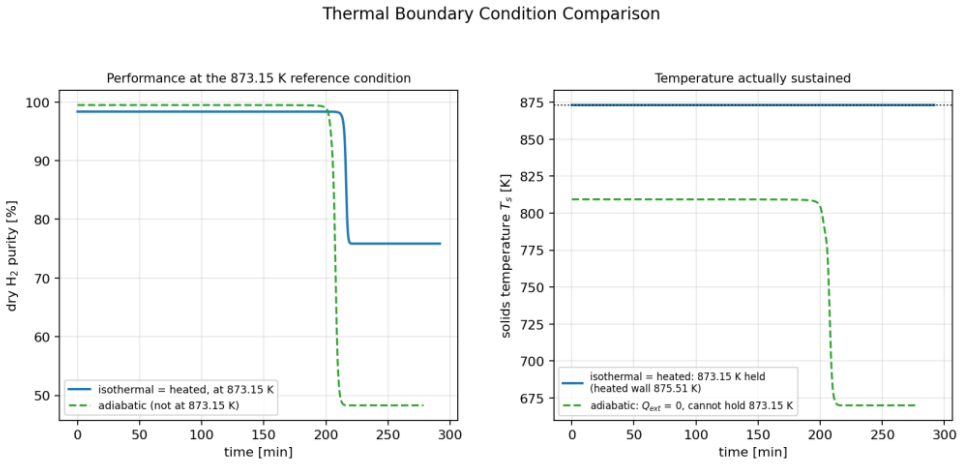


Figure 15 Sorbent conversion and carbonation rate versus time, with breakthrough onset, midpoint and completion marked.

Table 11 KU reactor energy channels with fresh sorbent at three times minimum fluidisation. The reactor only; no calciner or loop terms are included.

Channel	Isothermal (T_s = 873.150 K)	Adiabatic (Q_{ext} = 0)	Heated (T_s = 873.150 K, wall 875.503 K)
Solids temperature T_s [K]	873.150	809.349	873.150
R_1 steam methane reforming [W]	28.266	28.909	28.266
R_2 global reforming [W]	9.331	8.959	9.331
R_3 water-gas shift [W]	−4.430	−4.742	−4.430
Reforming absorbed, sum [W]	33.166	33.126	33.166
Carbonation released [W]	29.022	30.559	29.022
Sensible enthalpy [W]	0.000	−2.567	0.000
External reactor duty [W]	4.144	0.000	4.144
True carbonation offset [%]	87.51	92.25	87.51
First-law residual [W]	4.3×10^{-14}	-1.3×10^{-7}	4.3×10^{-14}



Performance of the three thermal treatments, referenced to 873.15 K (pre-breakthrough values)
Isothermal and heated hold the reference temperature and give identical chemistry; adiabatic cannot hold it.

	Isothermal	Adiabatic (Q_{ext} = 0)	Heated (main KU case)
solids temperature [K]	873.15 (held)	809.03 → 670.05	873.15 (held, wall 875.51)
dry H_2 purity [%]	98.339	99.434	98.339
CH_4 conversion [%]	97.686	98.669	97.686
CO_2 capture [%]	97.675	99.573	97.675
external heater duty [W]	4.154	0.000	4.154
breakthrough onset [min]	213.90	203.49	213.90
breakthrough midpoint [min]	216.34	207.92	216.34
breakthrough completion [min]	218.16	211.20	218.16

Figure 16 Thermal boundary-condition comparison referenced to the 873.15 K operating condition. Isothermal and heated cases hold the same bed temperature and therefore give identical chemistry; the adiabatic case cannot maintain the set point without an external heater.

Table 12 KU velocity study in the heated thermal mode. Methane conversion is essentially flat, so it cannot discriminate between operating points; fluidisation margin is the binding constraint.

U/u_{mf}	H_2 purity [%]	CH_4 conv. [%]	CO_2 capture [%]	Midpoint [min]	Heater [W]	Regime
1.5	98.391	97.738	97.760	431.57	2.023	Bubbling
2.0	98.401	97.748	97.777	323.59	2.679	Bubbling
3.0	98.419	97.763	97.806	215.67	3.968	Bubbling
5.0	98.438	97.773	97.837	129.49	6.479	Marginal
8.0	98.401	97.684	97.786	81.39	10.200	Slugging

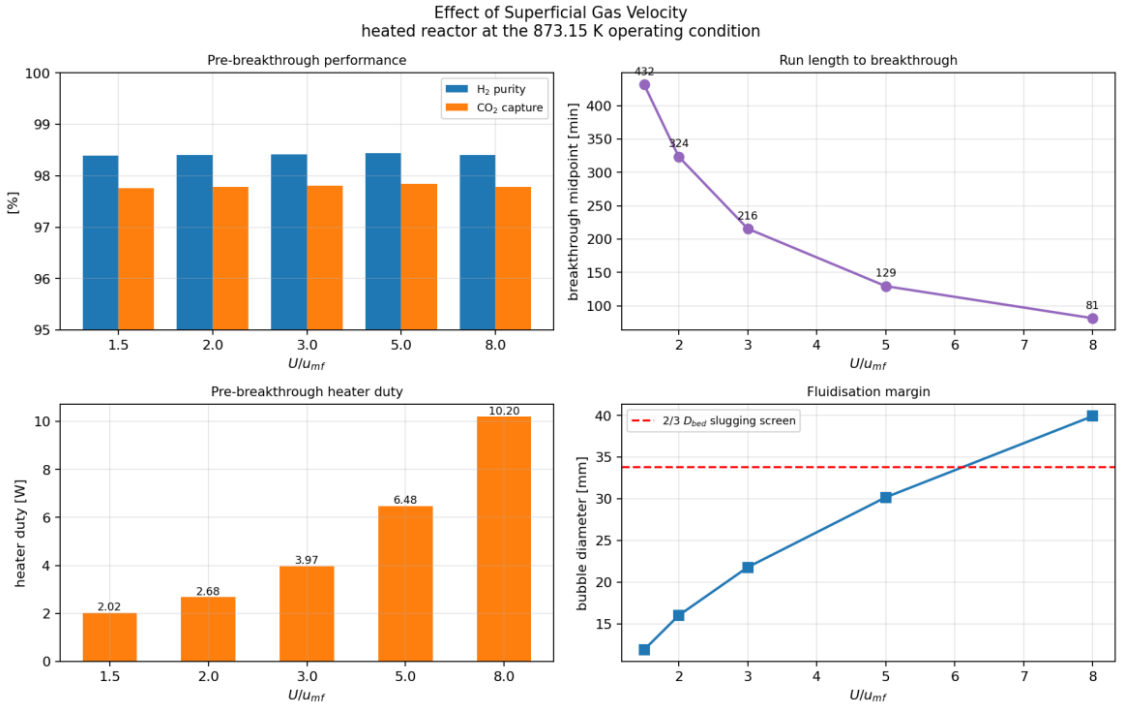


Figure 17 Effect of superficial gas velocity for the heated reactor at the 873.15 K operating condition. Pre-breakthrough performance changes little, whereas breakthrough time decreases and heater duty rises with throughput; the slugging margin becomes limiting at higher velocity.

Pre-breakthrough chemistry is essentially independent of velocity over 1.5–8 times minimum fluidisation: dry H_2 purity stays within 98.39–98.44%, methane conversion within 97.68–97.77%, and CO_2 capture within 97.76–97.84%. Velocity instead controls run length and heat demand, because a finite CaO inventory processes more reactant per unit time as throughput rises. The breakthrough midpoint falls from 431.6 min at $1.5u_{mf}$ to 81.4 min at $8u_{mf}$, while heater duty rises from 2.02 to 10.20 W. The fluidisation margin is the binding constraint: $5u_{mf}$ is marginal and $8u_{mf}$ crosses the slugging screen. Operation at $3u_{mf}$ was therefore retained as a practical nominal condition rather than being interpreted as a universally optimal velocity.

3.3.4 Model-to-model benchmark and verification status

The integrated KU BFB model is not directly experimentally validated. To provide an independent whole-reactor check, the final model was benchmarked against the published bubbling-fluidised-bed SE-SMR CFD model of Di Carlo et al. [24]. Di Carlo et al. also report a preliminary comparison of their CFD model with pilot-scale measurements, which strengthens the reference model, but the experimental support does not carry over to the KU model.

For the benchmark, the KU geometry and operating inputs were changed to match the Di Carlo case: 0.250 m reactor internal diameter, 0.400 m static bed height, 923 K, 101.325 kPa, 25 mol% CH_4 / 75 mol% H_2O (S/C = 3), 500 μm particles, 1880 kg m^{-3} particle density and superficial velocities of 0.2–0.5 m s^{-1}. The comparison uses fully calcined inlet sorbent. No kinetic constant, correction factor, hydrodynamic correlation or numerical tolerance was tuned to improve agreement.

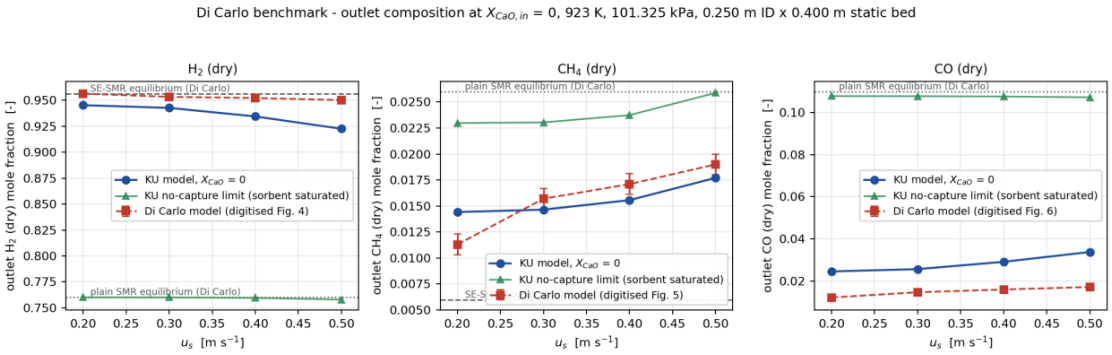


Figure 18 KU model predictions compared with the Di Carlo CFD benchmark for dry-basis outlet H_2, CH_4, and CO as a function of superficial gas velocity at 923 K, 101.325 kPa, and fully calcined inlet sorbent.

Hydrogen, the dominant dry-gas species, agrees within 1.11–2.77 percentage points across the four velocities. Methane differs by no more than 0.31 percentage points, while the absolute carbon-monoxide difference is 1.10–1.66 percentage points. The direction of the velocity trend is reproduced for all three species. In the saturated-sorbent/no-capture limit at 0.5 m s^{-1}, the KU model also closely recovers the plain-SMR limiting composition reported by Di Carlo.

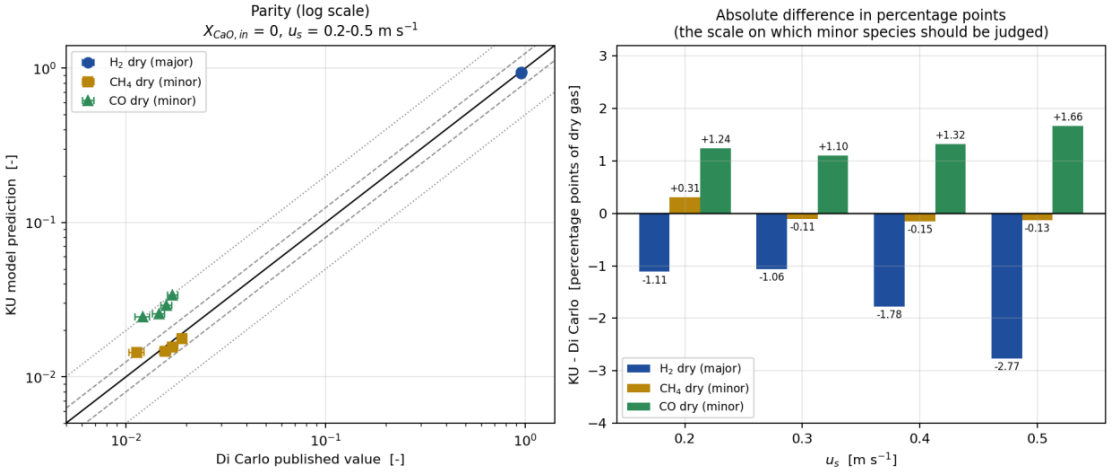


Figure 19 KU–Di Carlo benchmark parity and absolute outlet-composition differences. Percentage-point differences are used for the minor CH_4 and CO species because relative errors are misleading when the reference fractions are small.

The benchmark shows reasonable model-to-model agreement under matched conditions and does not reveal a clear implementation error requiring a change to the submitted KU model. Exact identity is not expected because Di Carlo uses a two-dimensional Eulerian-Eulerian CFD formulation with bifunctional particles, whereas the KU model is a one-dimensional reduced-order bubbling-bed model. This remains a model-to-model benchmark, not direct experimental validation of the KU reactor.

4 Discussion

4.1 What the progression between models actually established

The three phases of this practicum are often described as a sequence of increasingly complex reactors, but that is not quite the right reading. What actually progresses is the amount of the physics that has to be established independently at each stage, and the amount of external evidence available to check it.

The fixed-bed phase had a published reference model with the same geometry, feed and operating basis, so its correctness could be assessed directly against reported values, as set out in subsection 3.1. The circulating fluidised-bed phase has no such target. There is no published case with the same geometry, feed, and solids loop against which the final case could be checked, so its correctness rests on two things instead: the fact that its chemistry and energy treatment had already been benchmarked in the fixed-bed phase, and the internal conservation and consistency checks described in subsection 2.9 and reported for the final case in subsubsection 3.2.1. That is a weaker form of evidence and is presented as such throughout this report.

Table 13 sets the four model architectures side by side, because the differences between them are easy to blur once the results are read in sequence.

4.2 Interpreting the fixed-bed benchmark

Both the ODE and the DAE implementations reproduce the published trends, and the principal conversion, hydrogen-yield and hydrogen-purity values are generally close to the reference results. One feature of the final benchmark deserves comment beyond the numbers themselves: the residual disagreement with the reference model is not uniform across the performance indicators.

Conversion, hydrogen yield and purity are reproduced closely; the carbon capture ratio is the indicator that drifts, and it drifts most in the case with the highest propane content. That pattern is informative. Conversion and yield are integrals of what happens in the hot reforming zone, where the chemistry is fast and where small differences in transport properties matter little. The capture ratio also depends on where the carbonation front sits, how sharp it is, and how much carbon leaves unconverted as methane or carbon monoxide, all of which are sensitive to the temperature field. Since the temperature field is precisely what the substituted Multiflash properties influence, through the gas-solid heat-transfer coefficient, the axial thermal conductivity, and the Ergun term, it is unsurprising that the capture ratio carries most of the residual error.

The propane case compounds this because it has the hottest carbonation zone and carbonation is equilibrium-limited, making its capture the most temperature-sensitive quantity in the entire study. It is also the case that both independent implementations deviate in the same direction and by a similar magnitude, approximately -4.5 and -3.9 percentage points. Two implementations that share no code but do share the same substituted property correlations and the same underlying kinetic parameters would be expected to fail in the same direction if the cause lies in those shared inputs rather than in either implementation. That is the most plausible reading of the evidence available, though it cannot be proven without the original property package. The discrepancy is therefore reported transparently as a limitation of the present models rather than adjusted or explained away.

4.3 Significance of the circulating-bed inventory result

The inventory study produced a result that is easy to state and easy to over-claim, so both need care.

The model shows that increasing static solids hold-up, with circulation held constant, extends

Table 13 Comparison of the four model architectures developed or used in this practicum. The circulating and bubbling fluidised-bed models are physically distinct and are not variants of one another.

Feature	Fixed-bed ODE	Fixed-bed DAE	SER-CFB	KU BFB
Purpose	Reproduce the published fixed-bed model	Reproduce it retaining algebraic structure	Continuous SER / calcium-looping development framework	Pilot-scale modelling framework for the KU rig
Reactor regime	Packed fixed bed	Packed fixed bed	Dilute circulating transport riser	Bubbling fluidised bed
Steady or dynamic	Dynamic	Dynamic	Steady state	Quasi-steady gas, transient solid
Spatial representation	1-D axial, method of lines	1-D axial, method of lines	1-D axial march	1-D axial, two gas phases
Solver	SciPy `solve_ivp`, BDF	CasADi with SUNDIALS-IDAS	`scipy.integrate.solve_ivp`, stiff IVP	Stiff IVP with root-found solids temperature
Hydrodynamics	Fixed packing, Ergun pressure drop	Fixed packing, algebraic Ergun	Dense/lean solids profile from inventory closure	Wen–Yu, Haider–Levenspiel, Darton, K–L exchange
Catalyst treatment	Film substituted, kinetics at bulk gas	Film balance solved algebraically	Algebraic gas-film surface state	Kinetics on emulsion composition, catalyst inventory only
Sorbent treatment	Axial conversion field $X(z,t)$, film in closed form	Axial conversion field with algebraic film	Circulating population with contact factor	Single well-mixed global conversion $X(t)$
Solids circulation	None	None	Continuous catalyst and sorbent	None
Calciner	None	None	Algebraic ideal control volume	None
Experimental status	Model-to-model benchmark only	Model-to-model benchmark only	No experiment-specific validation	Model-to-model benchmark vs Di Carlo; no direct KU experimental validation
Main role in practicum	Independent reproduction and cross-check	Final benchmark authority for Phase I	Continuous-process development study	Pre-experimental modelling framework

the solids-rich contact region and improves carbon capture. The mechanism is contact rather than capacity: no additional regenerated sorbent is being supplied, and the sorbent circulation rate is unchanged, so the improvement cannot come from having more fresh capture capacity available per unit time. It comes from carbon dioxide generated further along the riser, which encounters a higher local sorbent concentration than it otherwise would. That interpretation was tested rather than assumed, through pressure-treatment variations and a mechanism-decomposition study that separated the hydrodynamic contact effect from a possible sorbent-aging artefact.

The engineering reading is more equivocal than the capture number alone suggests. A gain of 2.87 percentage points in the carbon capture ratio was achieved with 141.6 tonnes of additional static solids hold-up and a 50% increase in pressure drop. Whether that trade is worth making depends on the loop pressure balance, the standpipe and loop-seal design, the solids-handling power, and the capital cost of the additional solids inventory, none of which is inside the present energy boundary. The specific thermal duty being essentially unchanged, at approximately 11.67 kWh_{th} per kilogram of hydrogen, is a genuine finding, but it applies only to the reactor-calciner loop and does not mean the change is free at the plant level.

It also has to be said clearly that the final case is a modelling selection, not a demonstrated operating point. It is the case adopted as the reference for the present reduced-order model

because it represents a defensible compromise between contact and hydrodynamic cost within that model's own closure. It has not been shown to be achievable in any physical equipment, and specifically not in the KU rig, whose geometry it does not represent.

A one-dimensional model remains useful for rapid parametric studies and for identifying first-order relationships between solids inventory, reaction, heat transfer and carbon capture; however, its predictive capability is limited for a large circulating fluidised bed. Real CFB reactors can exhibit radial and circumferential variations in gas velocity, solids concentration, clustering, recirculation, wall effects and gas-solid contact that cannot be resolved by an axial one-dimensional representation. The present SER-CFB model should therefore be regarded as a reduced-order engineering framework and a baseline for further development. If this research is continued at PhD level, the current model can provide the starting point for a geometry-specific, experimentally supported model incorporating higher-dimensional CFD to resolve detailed CFB hydrodynamics and scale-up behaviour.

4.4 Why the CFB and KU models must remain separate

The temptation to merge the two fluidised-bed models is real, because they share chemistry, share a code lineage and were built by the same person within months of each other. They must not be merged because they describe different machines.

The circulating model assumes a riser with continuous solids circulation, a return path and a calciner that regenerates sorbent and returns it hot. Every one of those assumptions does work in the model: the dense/lean profile presumes transport-riser operation, the sorbent population presumes cycling, the energy ledger presumes hot returning solids, and the calciner closes the calcium balance. The KU rig has none of that hardware. Applying the circulating model to it would not merely be inaccurate, it would import an energy ledger for equipment that does not exist and a sorbent regeneration path that nothing in the rig can provide.

The KU model therefore rebuilds the physics on the assumptions that do hold. Its solids are well-mixed rather than circulating, so the sorbent state is a single global conversion rather than a population across cycle numbers. Its gas divides between bubble and emulsion phases rather than dense and lean zones. Its energy accounting stops at the reactor boundary because there is no loop to account for. Its performance ends in capacity exhaustion because nothing regenerates the inventory.

That difference also explains the most conspicuous contrast in the results. The KU model reports 97.7% methane conversion and 98.4% purity with fresh sorbent, considerably above what the circulating model achieves, and it would be a serious misreading to conclude that the bubbling configuration outperforms the circulating one. The KU numbers describe a small bed with a high sorbent-to-catalyst ratio at the start of a run that will terminate in a few hours. The circulating numbers describe a continuous process at industrial flow basis. They are not comparable quantities, and no comparison between them is offered anywhere in this report.

5 Limitations and Future Work

5.1 Limitations of the fixed-bed models

The reference model used 140 equally spaced axial nodes and reported negligible influence from further grid refinement; the final results presented here were therefore generated using the same spatial resolution. Small numerical differences from the published results remain because the present implementation uses different numerical solvers, thermophysical-property correlations, and, in the ODE formulation, several simplified algebraic treatments. At the reference grid,

however, the principal performance indicators show close agreement with the published model.

The substitution of explicit property correlations for the original Multiflash property package is an unavoidable source of difference. The adopted correlations are physically appropriate and transparent, but they cannot reproduce the internal Multiflash property values exactly. These differences can influence calculated heat transfer, mass transfer, pressure drop, diffusivity, and consequently the axial reactor profiles. The largest single discrepancy in the benchmark, the carbon capture ratio of the 15% propane case, is reported transparently on this basis rather than reconciled.

The ODE implementation contains additional documented approximations. Catalyst-surface concentration is approximated using the bulk-gas concentration, inlet pressure is used in the evaluation of kinetic partial pressures, the inlet boundary treatment is simplified, and representative-state values are used in part of the diffusivity calculation. These approximations reduce computational cost while maintaining close agreement with the reference model, but they also explain why the ODE results show slightly greater deviation than the DAE formulation.

The verification scope is limited to reproduction of published model results. The original reference work compared its model with laboratory breakthrough data, whereas the implementations developed in this practicum were not independently fitted or validated against new experimental measurements. In addition, the simulations represent only the reforming/carbonation step and do not describe the complete cyclic process, including depressurisation, sorbent regeneration, repressurisation, repeated cycling, or long-term sorbent degradation.

5.2 Limitations of the SER-CFB model

The present model is a steady-state, one-dimensional, reduced-order representation of a circulating fluidised-bed SER system coupled to an algebraic ideal calciner. It does not resolve radial solids segregation, core-annulus flow, particle clustering, cyclone separation, standpipe and loop-seal behaviour, calciner residence time and kinetics, particle attrition, catalyst deactivation, sulfur poisoning, coke formation, or reactor start-up and transient behaviour. In addition, no dedicated SER-CFB reactor geometry was available for this phase of the work; consequently, the riser geometry and hydrodynamic structure were inherited from the Romano-based carbonator framework [14]. The resulting predictions should therefore be interpreted as process-level modelling results rather than design predictions for a specific reactor. The complete SER-CFB formulation has also not been experimentally validated against a dedicated SER-CFB facility.

The reaction and transport submodels introduce additional uncertainty. The Xu–Froment kinetics [3] were originally developed for fixed-bed methane steam reforming and are applied here within a reduced-order fluidised-contact framework. Particle heat transfer is represented using the Gunn correlation [18], while gas-solid mass transfer is described using a single-particle correlation based on the adopted slip-velocity treatment [19]. Some of these correlations are therefore used outside, or close to the limits of, their original range of application. Sensitivity testing nevertheless showed that large changes in the assumed particle heat-transfer coefficient produced negligible changes in the principal performance indicators under the selected operating conditions. The catalytic source formulation also does not include the explicit contact de-rating factor applied to carbonation; this asymmetry had negligible numerical influence for the selected case because the dense-zone contact factor remained close to unity, but it remains a limitation of the present model formulation.

5.3 Limitations of the KU BFB model

The KU model is based on the geometry and operating concept of an existing pilot-scale bubbling fluidised-bed reactor. Its main limitation is therefore not the absence of a physical reactor basis, but that several parameters required for a fully specified model had not yet been provided or confirmed during the present study. Available equipment information was used wherever possible, while literature-based or provisional values were introduced only for parameters that remained unavailable. These assumptions introduce uncertainty into the quantitative predictions and should be replaced by measured KU values as further reactor information becomes available.

The available equipment information defines the principal reactor sections, including the 32 in straight bed section, 3 in transition section, and 4 in disengagement section. The supplied section dimensions sum to 39 in, while a 36 in heated length is reported separately. These quantities may refer to different physical extents; therefore, the exact heated region should be confirmed against the equipment documentation to ensure the wall-heating boundary is represented accurately.

Several hydrodynamic inputs remain provisional. In particular, the particle diameter of 150 µm is currently an assumed development value rather than a measured KU value and has a strong influence on the calculated minimum fluidisation velocity and subsequent bubble behaviour. Particle density, sphericity, minimum-fluidisation voidage, and the bed height at minimum fluidisation also require confirmation against the actual catalyst and sorbent inventory used in the pilot plant. Distributor geometry and distributor pressure-drop data were not available during this work, so the distributor is not represented explicitly. Consequently, predictions of bubble diameter, bubble-emulsion interchange, bed expansion, and the approach to slugging should be regarded as model estimates until these physical parameters are confirmed.

The sorbent and reaction descriptions also contain provisional parameters. The sorbent-to-catalyst ratio used in the model should be confirmed against the actual KU loading, while the carbonation capacity and kinetic parameters, including X_{max} and k_{carb}, are presently taken from the reference SER formulation rather than measured directly for the sorbent used in the KU reactor. These quantities directly influence CO_2 capture and the predicted breakthrough time. Experimental characterisation of the actual sorbent would therefore improve the reliability of the transient predictions.

The bubbling-bed hydrodynamics are represented using a reduced bubble-emulsion model. The formulation captures the principal effects of minimum fluidisation, bubble growth, bed expansion, and bubble-emulsion gas exchange, but does not resolve the full three-dimensional structure of the pilot bed. Local variations associated with bubble paths, cloud and wake regions, radial solids distribution, wall effects, and local gas-solid contact are therefore represented through correlations rather than resolved directly. The solids inventory and solids temperature are also treated using spatially averaged quantities.

The present model represents the existing KU reactor as a finite-inventory bubbling fluidised bed. Continuous sorbent regeneration is not included because the present pilot configuration does not contain the circulating solids loop and calciner represented in the separate SER-CFB model. Similarly, no explicit solids entrainment-loss balance is currently included because measured solids-loss data were not available. These simplifications are appropriate for the present model scope but should be reconsidered if the pilot system is later modified for continuous solids circulation or regeneration.

The transient formulation uses the average sorbent conversion as the state variable. At each sorbent state, the gas phase is solved quasi-steadily and the average sorbent conversion is then advanced in time. This provides a computationally efficient representation of the progression from fresh sorbent to breakthrough, but it does not resolve local distributions of sorbent age or

conversion within the bed. Predicted breakthrough time is therefore sensitive to the assumed sorbent inventory, maximum conversion, and carbonation kinetics.

Finally, although the model is based on a real KU pilot plant, the present implementation has not yet been validated against experimental operating data from that reactor. This distinction is important: the physical reactor exists and provides the geometrical basis of the model, but predictions of methane conversion, hydrogen purity, CO_2 capture, breakthrough time, heater duty, and hydrodynamic behaviour have not yet been confirmed against measured KU results. The Di Carlo comparison provides a model-to-model benchmark under matched conditions, not experimental validation of the KU reactor. Future measurements of particle properties, actual bed inventory, pressure drop, temperature, outlet-gas composition, and breakthrough behaviour would allow the model to be progressively calibrated and validated.

5.4 Future work

The immediate priority is direct experimental comparison with the KU pilot reactor. The Di Carlo benchmark provides an independent published-model comparison, but it does not constitute validation of the KU model. Experimental operation of the pilot plant should therefore be used to assess the predicted pre-breakthrough hydrogen-rich plateau, breakthrough and capacity-exhaustion behaviour, heater duty required to maintain the nominal operating temperature, and the influence of superficial gas velocity on sorbent run length and fluidisation behaviour. These measurements would also allow the presently assumed particle, inventory, and hydrodynamic parameters to be replaced by measured KU values.

The next major step is the introduction of ladle furnace slag (LFS) [23]. Once the KU pilot reactor is operated using LFS, the experimental reactor data, together with dedicated material-characterisation measurements, can be used to determine or calibrate the parameters required to describe LFS carbonation and regeneration. These include carbonation capacity, carbonation and calcination kinetics, cyclic degradation [22], particle properties, attrition behaviour, and relevant structural characteristics. The resulting LFS formulation can then be implemented in the KU model, and its predictions can be compared directly with the LFS experiments. This provides a controlled way to assess LFS as a potential replacement for conventional CaO rather than assigning unverified LFS parameters in advance.

This also creates a natural link between the pilot-scale KU model and the larger SER-CFB model. The KU reactor provides the pilot-scale experimental and model-validation pathway for developing the sorbent reaction description, while the SER-CFB model provides the baseline for larger-scale continuous operation. If LFS demonstrates satisfactory CO_2-capture capacity, reaction rate, stability, and cyclic performance at pilot scale, its experimentally supported kinetic and physical parameters can be transferred into the CFB framework to study the effects of solids inventory, circulation rate, reactor scale, carbon capture, and hydrogen production under continuous operation.

Continuous SER operation should therefore be treated as a subsequent integration stage rather than imposed directly on the present KU geometry. The existing KU pilot reactor does not contain the riser, loop seal, solids-return circuit, and calciner required for a continuous calcium-looping system. The SER-CFB model developed in this work provides the more appropriate baseline for that stage. Future development should introduce a defined reactor geometry, a more detailed calciner model, closure of the calcium circulation balance, and complete energy coupling between the carbonator, calciner, and solids-return system.

Higher-dimensional CFD could subsequently be used to investigate hydrodynamic effects that cannot be resolved by the present one-dimensional formulations, including radial solids

distribution, particle clustering, wall effects, gas-solid slip, and local reaction and heat-transfer fields. Such models do not by themselves provide validation; higher-dimensional formulations should ultimately be supported by experimental evidence.

A further stage would extend the analysis from reactor performance to the complete process. The thermal duties reported in the present work are limited to the defined reactor and solids-loop boundaries. Future system-level analysis should include heat recovery, steam generation, solids-handling requirements, blower and compressor electricity, calciner energy demand, and CO_2 compression. This would allow the technical advantages observed at reactor level to be translated into overall process efficiency and, subsequently, techno-economic performance.

Taken together, the present models establish a staged research pathway. The CaO-based KU model provides the initial pilot-scale baseline; KU experiments can validate the reactor formulation and subsequently support development of an experimentally supported LFS model; and the SER-CFB framework can then be used to investigate the potential of the validated sorbent under larger-scale continuous operation. This progression provides a clear baseline for further postgraduate research toward experimentally validated sorbent modelling, continuous SER development, scale-up, and ultimately detailed CFD and process-level assessment.

6 Conclusion

This practicum developed three connected reactor-modelling frameworks for sorption-enhanced reforming, progressing from reproduction of a published fixed-bed model, through integration of SER chemistry with a circulating fluidised-bed framework, to development of a model based on the existing KU pilot-scale bubbling fluidised-bed reactor.

The first phase independently reimplemented the published one-dimensional dynamic adiabatic fixed-bed SER model using two numerical formulations: a method-of-lines ODE model solved with SciPy and a semi-explicit index-1 DAE model solved with CasADi and SUNDIALS-IDAS. Final benchmarking was performed using the same 140-node axial resolution as the reference model. The DAE formulation reproduced the principal published performance indicators closely, while the independently developed ODE formulation followed the same trends with only small additional deviations resulting from its simplified algebraic treatment. The largest remaining discrepancy, in the carbon capture ratio of the 15% propane case, is reported transparently as a limitation rather than adjusted. This phase established the reforming kinetics, carbonation treatment, transport relations, energy balances and numerical framework subsequently used in the later models.

In the second phase, the SER chemistry and non-isothermal treatment were integrated with a Romano-based circulating fluidised-bed carbonator and hydrodynamic framework. The resulting steady-state, one-dimensional SER-CFB model represents a large-scale continuous system with solids circulation and an algebraic ideal calciner. Increasing only the static solids inventory by 50% extended the dense solids-rich region from 3.09 to 7.10 m and increased the carbon capture ratio from 68.80% to 71.68%, while methane conversion, hydrogen yield, purity and production also improved modestly. The improvement was achieved with an essentially unchanged specific thermal loop duty of approximately 11.67 kWh_{th} per kilogram of H_2, but with a pressure-drop increase from 19.8 to 29.8 kPa and a substantially larger static solids hold-up. The final case therefore demonstrates the importance of solids distribution and inventory in maintaining effective carbonation contact, but it should be regarded as a model-development reference case rather than a demonstrated operating optimum. Because the geometry is inherited from the large-scale Romano-based framework rather than from a specific SER-CFB facility, absolute hydrogen production and inventory values are strongly dependent on the adopted scale.

The third phase developed a transient reduced-order model of the existing KU pilot-scale bubbling fluidised-bed reactor. The model combines bubbling-bed hydrodynamics, methane steam reforming, CaO carbonation, heat transfer and finite sorbent capacity to predict the evolution from fresh sorbent to breakthrough. At the nominal condition of 873.15 K and $3u_{mf}$, the model predicts a high-purity hydrogen-rich pre-breakthrough period with methane conversion, hydrogen purity and CO_2 capture close to 98%, followed by sorbent-capacity exhaustion after approximately 213–217 min. The velocity study showed that increasing superficial gas velocity has little benefit for the principal pre-breakthrough composition indicators over most of the bubbling regime, while it substantially shortens sorbent operating time and increases heater duty. This behaviour reflects the higher reactant throughput through a finite CaO inventory together with changing bubbling-bed hydrodynamics. Operation at $3u_{mf}$ was therefore retained as a practical nominal condition rather than being interpreted as a universally optimal velocity.

The KU formulation is based on a real pilot plant, but several physical and operating parameters were not yet available or confirmed during this work and were therefore represented using literature-based or provisional values. The Di Carlo comparison provides an independent model-to-model benchmark under matched operating conditions, but it does not constitute experimental validation of the KU reactor. Direct comparison with KU experimental measurements remains the most important next step, particularly for hydrodynamics, temperature, gas composition, heater duty and breakthrough behaviour.

Taken together, the three models provide a staged foundation for continued SER research. The fixed-bed work establishes a numerically verified reaction and transport basis; the KU pilot model provides the pathway for experimental validation and future development of sorbent-specific behaviour; and the SER-CFB model provides a reduced-order baseline for investigating continuous operation and larger-scale calcium looping. CaO presently provides the reference sorbent against which future KU experiments can be assessed. If ladle furnace slag demonstrates suitable carbonation, regeneration and cyclic behaviour experimentally, its measured kinetic and physical parameters can subsequently be incorporated into the KU model and then transferred into the CFB framework for larger-scale continuous-system studies.

The work therefore establishes a numerically verified modelling baseline, rather than a final predictive design tool, for future geometry-specific, experimentally supported and higher-dimensional development of sorption-enhanced reforming. This provides a clear route toward continued postgraduate research involving experimental validation, LFS sorbent development, continuous SER-carbonator-calciner integration, CFD-based hydrodynamic analysis and ultimately system-level energy and techno-economic assessment.

References

[1] A. Mostafa et al. “Sustainable Hydrogen Production via Sorption Enhanced Reforming of Complex Biorefinery Side Streams in a Fixed Bed Adiabatic Reactor”. In: *Industrial & Engineering Chemistry Research* 62 (2023), pp. 15884–15896. DOI: 10.1021/acs.iecr.3c02401.

[2] A. Mostafa et al. “Modelling of Methane Sorption Enhanced Reforming for Blue Hydrogen Production in an Adiabatic Fixed Bed Reactor: Unravelling the Role of the Reactor’s Thermal Behavior”. In: *International Journal of Hydrogen Energy* 48 (2023), pp. 26475–26491. DOI: 10.1016/j.ijhydene.2023.03.357.

[3] J. Xu and G. F. Froment. “Methane Steam Reforming, Methanation and Water-Gas Shift: I. Intrinsic Kinetics”. In: *AIChE Journal* 35.1 (1989), pp. 88–96. DOI: 10.1002/aic.690350109.

[4] M. V. Twigg. *Catalyst Handbook*. 2nd ed. Wolfe Publishing Ltd., 1989.

[5] S. I. Uskov et al. "Propane Pre-Reforming into Methane-Rich Gas over Ni Catalyst: Experiment and Kinetics Elucidation via Genetic Algorithm". In: *Energies* 13.13 (2020), p. 3393. DOI: 10.3390/en13133393.

[6] J. R. Fernandez, J. C. Abanades, and R. Murillo. "Modeling of Sorption Enhanced Steam Methane Reforming in an Adiabatic Fixed Bed Reactor". In: *Chemical Engineering Science* 84 (2012), pp. 1–11. DOI: 10.1016/j.ces.2012.07.039.

[7] E. H. Baker. "The Calcium Oxide–Carbon Dioxide System in the Pressure Range 1–300 Atmospheres". In: *Journal of the Chemical Society* (1962), pp. 464–470. DOI: 10.1039/JR9620000464.

[8] B. J. McBride, S. Gordon, and M. A. Reno. *Coefficients for Calculating Thermodynamic and Transport Properties of Individual Species*. Tech. rep. NASA-TM-4513. NASA, 1993.

[9] B. E. Poling, J. M. Prausnitz, and J. P. O'Connell. *The Properties of Gases and Liquids*. 5th ed. McGraw-Hill, 2000.

[10] R. Pfeffer. "Heat and Mass Transport in Multiparticle Systems". In: *Industrial & Engineering Chemistry Fundamentals* 3.4 (1964), pp. 380–383.

[11] N. Wakao, S. Kaguei, and H. Nagai. "Effective Diffusion Coefficients for Fluid Species Reacting with First Order Kinetics in Packed Bed Reactors and Discussion on Evaluation of Catalyst Effectiveness Factors". In: *Chemical Engineering Science* 33.2 (1978), pp. 183–187.

[12] E. N. Fuller, K. Ensley, and J. C. Giddings. "Diffusion of Halogenated Hydrocarbons in Helium: The Effect of Structure on Collision Cross Sections". In: *Journal of Physical Chemistry* 73.11 (1969), pp. 3679–3685. DOI: 10.1021/j100845a020.

[13] S. Ergun. "Fluid Flow through Packed Columns". In: *Chemical Engineering Progress* 48 (1952), pp. 89–94.

[14] M. C. Romano. "Modeling the Carbonator of a Ca-Looping Process for CO_2 Capture from Power Plant Flue Gas". In: *Chemical Engineering Science* 69.1 (2012), pp. 257–269.

[15] D. Kunii and O. Levenspiel. *Fluidization Engineering*. 2nd ed. Butterworth-Heinemann, 1991.

[16] D. Kunii and O. Levenspiel. "The K-L Reactor Model for Circulating Fluidized Beds". In: *Chemical Engineering Science* 55.20 (2000), pp. 4563–4570.

[17] C. Y. Wen and Y. H. Yu. "A Generalized Method for Predicting the Minimum Fluidization Velocity". In: *AIChE Journal* 12.3 (1966), pp. 610–612.

[18] D. J. Gunn. "Transfer of Heat or Mass to Particles in Fixed and Fluidised Beds". In: *International Journal of Heat and Mass Transfer* 21.4 (1978), pp. 467–476.

[19] W. E. Ranz and W. R. Marshall. "Evaporation from Drops". In: *Chemical Engineering Progress* 48 (1952), pp. 141–146, 173–180.

[20] A. Haider and O. Levenspiel. "Drag Coefficient and Terminal Velocity of Spherical and Nonspherical Particles". In: *Powder Technology* 58 (1989), pp. 63–70.

[21] R. C. Darton et al. "Bubble Growth Due to Coalescence in Fluidized Beds". In: *Transactions of the Institution of Chemical Engineers* 55 (1977), pp. 274–280.

[22] G. S. Grasa and J. C. Abanades. "CO_2 Capture Capacity of CaO in Long Series of Carbonation/Calcination Cycles". In: *Industrial & Engineering Chemistry Research* 45.26 (2006), pp. 8846–8851.

[23] P. Kumari et al. “Enhanced CO_2 Capture via Calcium Looping with Mesoporous Ladle Furnace Stainless Steel Slag”. In: *Carbon Capture Science & Technology* 14 (2025), p. 100354.

[24] A. Di Carlo et al. “Sorption Enhanced Steam Methane Reforming on Catalyst-Sorbent Bifunctional Particles: A CFD Fluidized Bed Reactor Model”. In: *Chemical Engineering Science* 173 (2017), pp. 428–442. DOI: 10.1016/j.ces.2017.08.014.

A Governing equation groups by model

Table 14 shows which equation groups are active in each of the three model families and in what form. It is intended as an orientation map for the detailed equations given in section 2; it does not repeat them.

Table 14 Equation groups active in each model family and the form in which they appear.

Equation group	Fixed-bed ODE/DAE	SER-CFB	KU BFB
Gas species balance	Dynamic PDE, convection + dispersion + film exchange	Steady axial ODE, plug flow, no dispersion	Steady axial ODE per phase, bubble and emulsion
Gas energy balance	Dynamic, exchange with both solids	Steady, exchange with catalyst and sorbent, wall and auxiliary	Bubble-phase axial balance with donor-upwinded transfer
Catalyst energy balance	Dynamic, film exchange + reaction heat	Steady, gas-catalyst transfer + reaction heat + wall	Combined into the well-mixed solids balance
Sorbent energy balance	Dynamic, film exchange + carbonation heat	Steady, includes sensible enthalpy of captured CO_2	Combined into the well-mixed solids balance
Inert heat-carrier balance	Present when inert pellets are used	Not used	Not used
Catalyst film mass transfer	Algebraic (DAE) / substituted (ODE)	Algebraic gas-film surface state	Not enabled; kinetics on bulk emulsion gas
Sorbent film mass transfer	Algebraic (DAE) / closed form (ODE)	Not represented separately	Not represented separately
Sorbent state	Axial field $X(z,t)$	Circulating population with contact factor	Single global $X(t)$
Pressure	Ergun, algebraic (DAE) / integrated (ODE)	$dP/dz = -\rho_{mix} g \varepsilon_s(z)$	Not resolved; distributor drop not modelled
Boundary conditions	Danckwerts (DAE) / Dirichlet (ODE)	Inlet feed construction, outlet calciner interface	Inlet feed; outlet to freeboard and filters
Bubble-emulsion exchange	Not applicable	Not applicable	Kunii–Levenspiel per species plus hydrodynamic crossflow
Hydrodynamic closure	Fixed packing, $\varepsilon = 0.4$	Dense/lean profile from inventory closure	Ar, Wen–Yu, Haider–Levenspiel, Darton, slugging screen
Calciner	Not applicable	Algebraic ideal control volume, five duty channels	Not applicable
Thermodynamics	NASA-7 gas, Kelley solids	NASA-7 gas, Kelley solids	Absolute formation-referenced enthalpies
KPI definitions	Integral to breakthrough	Steady-state outlet and loop duty	Integral at each sorbent state

B Fixed-bed equation-to-code map

Table 15 Equation-to-code map for the two independent fixed-bed implementations.

Equation group	Source	ODE location (`ser_model/`)	DAE location (`ser_dae/`)
Gas species and energy balances	[1] Table 1; [2] eqs 8, 12	`reactor.py::rhs`	`dae_model.py::_build`
Catalyst film balance	[2] eq 9	`reactor.py::compute_fields` (substituted)	`dae_model.py::_build` (film rows)
Sorbent film balance	[2] eq 10	`reactor.py` (closed-form β, surface CO_2)	`dae_model.py::_build` (film rows)
Sorbent conversion	[2] eq 11	`reactor.py::rhs`	`dae_model.py::_build` (X rows)
Velocity closure and Ergun	[2] eq 5; [13]	`reactor.py::compute_fields`; `transport.py::ergun_dPdz`	`transport.py::ergun_dPdz` (algebraic P)
Boundary conditions	[2] eq 20	Dirichlet in `reactor.py`	`boundary_conditions.py`
Xu–Froment, Uskov, carbonation	[3] eqs S6–S9; [4–7]	`kinetics.py`, `params.py`	`kinetics.py`, `params.py`, `equilibrium.py`
NASA-7 thermodynamics	[8, 9]	`nasa_thermo.py`, `thermo.py`	`thermo.py`
Transport correlations	[3] eqs S10–S15; [10–13]	`transport.py`, `thermo.py`	`transport.py`
Property substitutions for the unavailable package	[9]	`thermo.py`	`transport.py`
KPI definitions	[1] eqs 4–10	`postprocess.py`	`postprocess.py`
Case definitions	–	`cases.py`	`cases.py`
Entry point	–	`results_ODE.py`	`results.py`, `run_all_parallel.py`

C SER-CFB equation-to-code map

Table 16 Equation-to-code map for the integrated SER-CFB model.

Model element	Location
Continuous reactor-calciner loop, material and energy accounting	`model/ser_cfb/stage6_model.py`
Coupled axial species and three-phase energy solution	`model/ser_cfb/stage5_model.py`
Catalyst gas-film balance and surface-state calculation	`model/ser_cfb/chemistry/film.py`
Hydrodynamic solids profile and inventory closure	`model/ser_cfb/stage2_hydro.py`
Interphase heat transfer and energy source terms	`model/ser_cfb/energy/energy_model.py`
Links to the collaborator's carbonator framework and to the parent runtime	`model/ser_cfb/chemistry/matt_link.py`, `adapters/matt_legacy.py`, `chemistry/parent_link.py`
Case configuration	`model/ser_cfb/config.py`
Result and figure regeneration	`postprocess/generate_results.py`, `postprocess/generate_figures.py`
Conservation and stability verification	`verification/verify_model.py`
Entry point	`run_model.py`

D KU BFB equation-to-code map

Table 17 Equation-to-code map for the KU bubbling-bed model. Module roles follow the package structure and the KU source documentation; the release-verification script itself is not included in the delivered package, although its recorded output is.

Model element	Location
Section geometry, local diameter and area profile	`ku/geometry.py`
Species and mixture property data	`ku/properties.py`
Reacting-mixture properties, including the Herning–Zipperer viscosity used for the authoritative baseline	`ku/reacting.py` (`_props`)
Archimedes number, Wen–Yu u_{mf}, Haider–Levenspiel u_t, Darton bubble growth, holdup, bed expansion, slugging screen	`ku/hydrodynamics.py`
Two-phase bubble-emulsion structure and Kunii–Levenspiel interchange	`ku/bfb.py`
Two-phase species balances, hydrodynamic cross-flow, reforming and carbonation source terms, sorbent transient	`ku/reacting.py`
Energy balances and thermal modes	`ku/energy.py`, `ku/energy_eq.py`
Reactor solution and reproduction file	`run.py`
Figure regeneration on the final hot SER baseline	`make_report_figures.py`
Recorded release-verification results	`results/ku_reactor/ku_release_verification.json`

E Major input parameters

Table 18 lists the principal input parameters of the three model families. The status column distinguishes quantities supplied from equipment information, quantities inherited from the literature or from the reference SER formulation, quantities calculated by the models, and provisional or assumed development values. Provisional KU quantities are not measured experimental KU values.

Table 18 Principal input parameters of the three model families, classified by status. Provisional/assumed values are development values, not measurements.

Model	Parameter	Value	Status
Fixed bed	Reactor diameter / bed length	2.26 m / 5 m	Literature/inherited
Fixed bed	Feed temperature / pressure	550 °C / 10 bar	Literature/inherited
Fixed bed	Steam-to-carbon ratio / GHSV	4 / 350 N m^3 h^{-1} m^{-3}	Literature/inherited
Fixed bed	Initial solids temperature	850 °C	Literature/inherited
Fixed bed	Bed void fraction / X_{max}	0.4 / 0.4	Literature/inherited
Fixed bed	Inert heat carrier (when used)	alumina, 3950 kg m^{-3}, 0.88 kJ kg^{-1} K^{-1}	Literature/inherited
Fixed bed	Solid thermal conductivity	1.0 W m^{-1} K^{-1}	Provisional/assumed
Fixed bed	Final reported grid	N = 140	Literature/inherited
SER-CFB	Methane feed basis	2442.903053 mol s^{-1}	Calculated
SER-CFB	Riser height	40 m	Literature/inherited
SER-CFB	Gas inlet temperature	873.15 K	Literature/inherited
SER-CFB	Catalyst / sorbent return temperature	973.15 K / 1023.15 K	Literature/inherited
SER-CFB	Catalyst particle diameter, effectiveness	150 µm, η_{cat} = 1.0	Literature/inherited

Table 18 (continued)

Model	Parameter	Value	Status
SER-CFB	Carbonation contact decay β	6.62 m^{-1}	Literature/inherited
SER-CFB	Solids inventory, initial case / final case	283 103.2 kg / 424 654.8 kg	Calculated
SER-CFB	Superficial velocity (final case)	6.25 m s^{-1}	Calculated
KU BFB	Straight bed length / internal diameter	0.8128 m / 0.0508 m	Supplied
KU BFB	Transition cone length	0.0762 m (2.00 in → 3.75 in)	Supplied
KU BFB	Disengagement length / internal diameter	0.1016 m / 0.09525 m	Supplied
KU BFB	Operating temperature	873.15 K	Supplied
KU BFB	Heated-mode wall temperature	875.503 K	Calculated
KU BFB	Particle diameter	150 µm	Provisional/assumed
KU BFB	Voidage at minimum fluidisation	0.45	Provisional/assumed
KU BFB	Bed height at minimum fluidisation	0.20 m	Provisional/assumed
KU BFB	Calcium charged	5.4667 mol	Calculated
KU BFB	X_{max}	0.4	Literature/inherited
KU BFB	Carbonation rate constant k_{carb}	0.35 s^{-1}	Literature/inherited
KU BFB	Emulsion solids partition at $3u_{mf}$	0.51662 = 0.08610 catalyst + 0.43052 CaO	Calculated